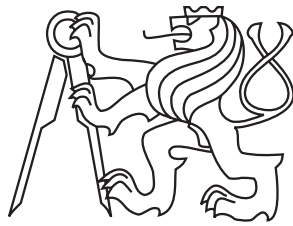Czech Technical University in Prague

Faculty of Nuclear Sciences and Physical Engineering

DIPLOMA THESIS

2012   Lenka Hrazdilová

Czech Technical University in Prague
Faculty of Nuclear Sciences and Physical Engineering

Meson-baryon resonaces generated within the chiral model framework

Meson-baryonové rezonance generované v rámci chirálního modelu

DIPLOMA THESIS

Author:	Bc. Lenka Hrazdilová
Supervisor:	RNDr. Aleš Cieplý, CSc
Year:	2012

Declaration

I declare that I wrote my research work independently and exclusively with the use of cited bibliography.

I agree with the usage of this thesis in the purport of the Act 121/2000 (Copyright Act).

Prague, May 7, 2012

....
Lenka Hrazdilová

Acknowledgements

Title: Meson-baryon resonaces generated within the chiral model framework

Author: Bc. Lenka Hrazdilová

Branch of study: Nuclear Engineering

Specialization: Experimental Nuclear Physics

Sort of projesct: Diploma thesis

Supervisor: RNDr. Aleš Cieplý, CSc

Nuclear Physics Institute AS CR, Řež

Abstract: The s-wave resonances that arise in kaon–nucleon interactions are examined in the framework of chirally motivated model and coupled channel approach. By solving Lippman–Schwinger equation with an interaction kernel in separable form for 10 meson–baryon channels $\pi\Lambda$, $\pi\Sigma$, $\bar{K}N$, $\eta\Lambda$, $\eta\Sigma$, and $K\Xi$ we search the dynamically generated resonances as poles of the scattering matrix on the unphysical Riemann sheets in the complex energy plane. The separable potential is derived from the effective chiral Lagrangian taken up to second order in external mesons momenta or considering only the leading Weinberg–Tomozawa interaction. Our objective is to study $S = -1$ strange baryon resonances with $I = 0$, 1 isospins in the energy range 1300-1800 MeV. We obtained satisfactory results on the $\Lambda(1405)$, $\Lambda(1670)$ and $\Sigma(1750)$ resonances. The analysis of pole movements into the zero coupling limit and to the limit of $SU(3)$ symmetry restoration provides additional insights into the pole origins.

Key words: dynamically generated resonances, meson–baryon interactions, chiral model, $\Lambda(1405)$

Název práce:	Meson-baryonové rezonance generované v rámci chirálního modelu
Autor:	Bc. Lenka Hrazdilová
Obor:	Jaderné Inženýrství
Zaměření:	Experimentální Jaderná Fyzika
Druh práce:	Diplomová práce
Vedoucí práce:	RNDr. Aleš Cieplý, CSc
	Ústav jaderné fyziky AV ČR, Řež

Abstrakt: Pomocí chirálního modelu a metody vázaných kanálů, zkoumáme s-vlnové rezonance, které vznikají v kaon–nukleonových interakcích. Řešením Lippman–Schwingerovy rovnice s interakčním jádrem v separabilním tvaru pro deset meson–baryových kanálů $\pi\Lambda$, $\pi\Sigma$, $\bar{K}N$, $\eta\Lambda$, $\eta\Sigma$ a $K\Xi$ hledáme dynamicky generované rezonance jako póly rozptylové matice na nefyzikálních Riemannových listech pro komplexní hodnoty energie. Separabilní potenciál je odvozen z efektivního chirálního lagrangiánu uvažovaného až do druhého řádu v externích hybnostech mezonů nebo pouze z členu představujícího Weinberg–Tomozawovskou interakci. V naší práci studujeme baryonové rezonance s podivností $S = -1$ a izospinem $I = 0$, 1 v rozsahu energií 1300-1800 MeV. Získali jsme uspokojivé předpovědi pro rezonance $\Lambda(1405)$, $\Lambda(1670)$ a $\Sigma(1750)$. Analýza pohybu pólů do limity nulové vazby a limity obnovení $SU(3)$ symetrie přináší nový pohled na podstatu rezonancí.

Klíčová slova:	dynamicky generované rezonance, mezon–baryonové interakce,
	chirální model, $\Lambda(1405)$

Contents

List of Figures

List of Tables

Chapter 1

Introduction

Baryon resonances play an important role in examining meson–baryon interactions at low energies. In this energy range, the perturbative approach of QCD is inapplicable due to a large value of the strong coupling constant and non-perturbative method is required. The convenient tool to deal with this problem is provided by chiral symmetry that governs interactions of the pseudoscalar mesons octet with the octet of baryons. In connection with coupled channel technique we have an excellent framework for an investigation of dynamically generated resonances appearing in kaon–nucleon interactions. The present work is focused on s-wave resonances with the $S = -1$ strangeness and the $I = 0$, 1 isospins in a range of energies around 1300–1800 MeV.

The chiral symmetry is an approximate flavour symmetry of strong interactions which holds exactly in the limit of vanishing quark masses. Thus it serves as a good approximation in the $SU(2)$ sector since current masses of the light u and d quarks are much lower then the hadron energy scale $m_u, m_d \ll 1$ GeV. Due to the fact that a mass of the strange s quark is much larger then masses of the light u and d quarks, the question whether the chiral symmetry is an appropriate and correct approach for the $SU(3)$ sector is still open. A exploration of chirally motivated models aimed at strange $S = -1$ baryon resonances could contribute to this issue.

Another important motivation for examining baryon resonances in context of chiral models is an existence of the $\Lambda(1405)$ resonance about 27 MeV below the K^-p threshold. The nature of this resonance has not been fully understood yet. Chiral $SU(3)$ calculations show this problem in a new perspective and describe this resonance as a typical example of dynamically generated state. Other approaches interpret the $\Lambda(1405)$ resonance as a $\bar{K}N$ bound state, pentaquark or exited baryon state in the constituent quark model.

In our work, we utilize an effective approach invented by Weinberg [13], based on substituting the QCD Lagrangian by an effective Lagrangian which is formulated in terms of meson and baryon fields and includes all terms preserving the chiral symmetry. A construction of a non-perturbative scattering amplitude is addressed by means of a coupled channel technique. Our models are based on a solution of the Lippman-Schwinger equation with a potential in a separable form which reflects the $SU(3)$ chiral symmetry and governs interaction of the pseudoscalar mesons octet $(\pi, K, \bar{K}, \eta)$ with the baryons octet $(N, \Lambda, \Sigma, \Xi)$. In this scheme, dynamically generated resonances appear due to the interactions of meson–baryon components in 10 coupled channels $\pi\Lambda$, $\pi\Sigma$, $\bar{K}N$, $\eta\Lambda$, $\eta\Sigma$, and $K\Xi$. These resonances then manifest themselves as poles of the scattering matrix on specific unphysical Riemann sheets of the complex energy manifold.

The chief aim of this study is to search these poles in our chirally motivated models up to energies around 1800 MeV classify them according to their mass, width and isospin, and assign them to experimentally measured resonances established in Particle Data Group (PDG)[11]. It is necessary to emphasize that all our models are fitted to the low energy $\bar{K}N$ data and thus we do not expect the models to work so well at higher energies. Particularly, we are concerned in the isoscalar states since in the sector with $I = 1$ isospin there is a lack of sufficient experimental data available and thus we can't competently qualify our results. Moreover we study the origin of the poles by following their movements on the complex energy manifold to the zero coupling limit and to the $SU(3)$ symmetry restoration limit. In this way, we are able to relate the observed poles to the pertinent channels and explore the octet and singlet states in the $SU(3)$ symmetry restoration.

The study of $S = -1$ strange baryon resonances in context of chirally motivated models and coupled channel approach was performed by several groups before [7], [9], [14], [15], [16], [17], [18], [19], [20], [21]. Our approach follows the Heavy Baryon formulation of chiral Lagrangian proposed in Ref. [22]. In this thesis, we employ few models developed by Cieply and Smejkal [6], [23], [10], based on the leading order Weinberg-Tomozawa interaction (WT) or including terms up to second order of chiral Lagrangian in external momenta. We compare our predictions obtained with updated models fitted to recent data from kaonic-hydrogen experiment SIDDHARTA with the results an older model based on DEAR measurement and with other theoretical models that adopt different techniques of coupled channel formalism.

The paper is organized as follows. The review of experimental observations and theoretical directions used in studies of s-wave baryon resonances with $S = -1$ strangeness

are summarized in Chapter 2. In the next chapter we briefly outline the framework of the effective phenomenological Lagrangians and chiral perturbation theory. The description of coupled channel approach and separable potentials used in our models follows in Chapter 4. In the end of this chapter we also overview other chirally motivated models based on similar approaches. Finally, in Chapter 5 we present results of our analysis and compare them with the experimentally measured resonances listed in the PDG and with some other theoretical models. The study of pole movements to the zero coupling limit and to the limit of $SU(3)$ symmetry restoration is covered there too.

Chapter 2

S-wave resonances in $S = -1$ sector

In this chapter, we go through experimental findings of the s-wave resonances in sector with strangeness $S = -1$. In order to compare our theoretical predictions with experimental data we discuss properties of these resonances as well as details of accomplished experiments. In this work, we are dealing with resonances with isospin $I = 0$ and $I = 1$ in the energy range 1300-1800 MeV. As we can see in the PDG tables [11], the resonances with isospin $I = 0$, $\Lambda(1405)$, $\Lambda(1670)$ and $\Lambda(1800)$ are well established baryons which properties are measured by various experiments. On the other hand, in sector with isospin $I = 1$ there is only one three star resonance $\Sigma(1750)$. The other resonances as $\Sigma(1480)$, $\Sigma(1560)$ and $\Sigma(1620)$ are given only one or two stars on the four stars scale. The experimental results related to these resonances are often inconsistent. Thus we will mostly concentrate on resonances with $I = 0$ isospin, with special care to the $\Lambda(1405)$ resonance.

In the last section of this chapter, we summarize the theoretical models that describe the $S = -1$ s-wave resonances with an emphasis on the quark model approach.

2.1   Lambda resonances

2.1.1 $\Lambda(1405)$

Lambda(1405) is an s-wave resonance with strangeness $S = -1$, isospin $I = 0$, negative parity and spin 1/2 that lies just below the $\bar{K}N$ threshold and decays via strong interaction into $\pi\Sigma$ channel, concretely into the $\pi^-\Sigma^-$, $\pi^+\Sigma^-$ and $\pi^0\Sigma^0$ channels. Since we are not able to observe the resonance directly, its properties have been extracted by analyzing the invariant mass distribution of the final state in production experiments.

First evidence of the resonance was found in the $K^-p \to \pi\pi\pi\Sigma$ reaction measured in bubble chamber experiment in 1961 [24]. The observed distribution of the invariant $\pi\Sigma$ mass was interpreted as a peak of resonance at 1405 MeV. Since that time, many other experiments have been accomplished. The overview of experimental results related to this resonance can be found in the PDG [11],[25].

The highest statistics of data and the most detailed analysis were performed by Hemingway [4] and Thomas *et al.* [3]. The first measurement was based on CERN bubble chamber experiment. The $\Lambda(1405)$ spectrum was reconstructed from invariant masses of 766 $\Sigma^+\pi^-$ events and 1106 $\Sigma^-\pi^+$ events which were observed in $K^-p \to \Sigma^+(1660)\pi^- \to (\Sigma\pi\pi)^+\pi^-$ reaction at 4.2 GeV/c. In this analysis, a selection rule 1600 MeV $\leqq M(\Sigma\pi\pi)^+ \leqq$ 1720 MeV for invariant mass of $\Sigma^+(1660)$ was used. The mass and width of $\Lambda(1405)$ were determined to be 1391 ± 1 MeV and 32 ± 1 MeV. The peak was fitted by the Breit-Wigner formula, but the fit was very poor. Beside that a bump of $\Lambda(1405)$ was found to be asymmetric with a rapid fall in intensity as the $\bar{K}N$ threshold energy is approached and the peak for the $\Sigma^+\pi^-\pi^+$ final states has a different shape that the one for the $\Sigma^-\pi^+\pi^+$. A similar shape was found analysis [3] based on the $\pi^-p \to K^0(\Sigma^\pm\pi^\mp)$ reaction at 1.69 GeV/c. However, the fall-off at the $\bar{K}N$ threshold was slightly different. In this work, all 400 $\Sigma^\pm\pi^\mp$ events were used for analysis (no selection rules for background correction). Various fits of Hemingway's data (in Ref. [4]) based on M-matrix, K-matrix and separable potentials in the $(\pi\Sigma, \bar{K}N)$ coupled channels were compared in [26]. In that work, the best fit for mass and width gave 1406.5 ± 4.0 MeV and 50 ± 2 MeV, respectively.

The reason for continuing research of the $\Lambda(1405)$ lineshape in modern experiments is an examination of the $\Lambda(1405)$ nature. Chiral models explain the $\Lambda(1405)$ resonance as a superposition of two states. In zero coupling limit, one state corresponds to resonance in the the $\pi\Sigma$ channel, the second state corresponds to quasi-bound state in the $\bar{K}N$ channel. The states should be populated differently in various decay schemes. Since the $\pi^-\Sigma^+$ and $\pi^+\Sigma^-$ spectra consists not only of the $I = 0$ component, but also $I = 1$ component (neglecting the small $I = 2$ component), it is necessary to deal with a contamination of the spectra by the $\Sigma(1385)$ resonance. Nowadays, it is assumed that the difference of charged $\pi^-\Sigma^+$ and $\pi^+\Sigma^-$ spectra is caused by mixing of states with $I = 0$ and $I = 1$ amplitude, see review [27]. Since isospin forbids decay of $\Sigma(1385)$ into purely isoscalar $\pi^0\Sigma^0$ channel, the ideal channels for studying $\Lambda(1405)$ should be the $\pi^0\Sigma^0$ channel.

A photoproduction of $\Lambda(1405)$ was measured at Spring-8/LEPS facility. The $\Lambda(1405)$ lineshape was investigated in the charged $\pi\Sigma$ channels through $\gamma p \to K^+\Lambda(1405) \to$

$K^+\pi^\pm\Sigma^\mp$ reaction at 1.5-2.4 GeV [2]. They used kinematical and geometrical cut-offs requiring the K^+ and the pion coming from the same vertex, and that the K^+ should not decay in flight. The resulting $\pi^+\Sigma^-$ and $\pi^-\Sigma^+$ spectra were different. Such findings indicate a strong mixing of the isospin 0 and 1 terms of the $\pi\Sigma$ scattering amplitudes. Next experiment performed at the LEPS facility utilized the same reaction. The results again showed different mass distributions of $\pi^+\Sigma^-$ and $\pi^-\Sigma^+$ [1]. Nevertheless the line-shape was not consistent with the previous measurement, as one can see in the Fig. 2.1 taken from Ref. [1]. The contamination by $\Sigma(1385)$ was handled in a the following way. Since the production of $\Sigma^0(1385)$ was measured also in the $K^+\Lambda\pi^0$ final state, which is prohibited by isospin conservation for $\Lambda(1405)$ decay, the $\Sigma(1385)$ contamination in the $K^+\pi^\pm\Sigma^\mp$ invariant mass could be estimated from the $K^+\Lambda\pi^0$ final state. The production ratio of $\Lambda(1405)$ to $\Sigma^0(1385)$ and the differential cross sections for photoproduction of these hyperon resonances were obtained for photon energies in the region near production threshold, $1.5 < E_\gamma < 2.0$ GeV, and above, $2.0 < E_\gamma < 2.4$ GeV.

The $K^-p \to \pi^0\pi^0\Sigma^0$ channel for studying the $\Lambda(1405)$ spectrum is complicated to analyze due to the two identical particles in final state. The resulting peak located at 1420 MeV obtained by the Crystal Ball Collaboration (Ref. [28], [29]) from this reaction was not used for the PDG averages.

The $pp \to pK^+\Lambda(1405) \to pK^+\pi^0\Sigma^0$ reaction has been studied at COSY-Julich by using a 3.65 GeV/c proton beam incident on a hydrogen target [5]. The resulting extracted spectrum of $\pi^0\Sigma^0$ is in agreement with Thomas *et al.* [3] and Hemingway [4]. The three experimental spectra are compared in Fig. 2.2 taken from [5].

To summarize, even though plenty of $\Lambda(1405)$ measurements were already performed, the available experimental data are not sufficient for comparing theoretical predictions with the lineshape of this resonance. It is obvious that the $\pi^-\Sigma^+$, $\pi^+\Sigma^-$ and $\pi^0\Sigma^0$ spectra differ which is not indicated by a simple quark model picture. If $\Lambda(1405)$ were pure single quantum state (three quark state), its lineshape should be independent of the decay scheme.

Most recent experiments measure the $\Lambda(1405)$ spectrum using photoproduction $\gamma p \to K^+\Lambda(1405) \to K^+\pi\Sigma$ and the π^- induced reaction $\pi^-p \to K^0\Lambda(1405) \to K^0\pi\Sigma$ [30]. These measurements are designed to test the two pole structure of the $\Lambda(1405)$ resonance. The first reaction is suited to isolate the second pole of the $\Lambda(1405)$ which couples dominantly to the $\bar{K}N$ channel whereas the second favors the first pole of the $\Lambda(1405)$ [31]. The the strength and shape of the $\Lambda(1405)$ resonance was studied in context of chiral unitary approach using the radiative production with a kaon beams $K^-p \to \gamma\Lambda(1405) \to \gamma MB$
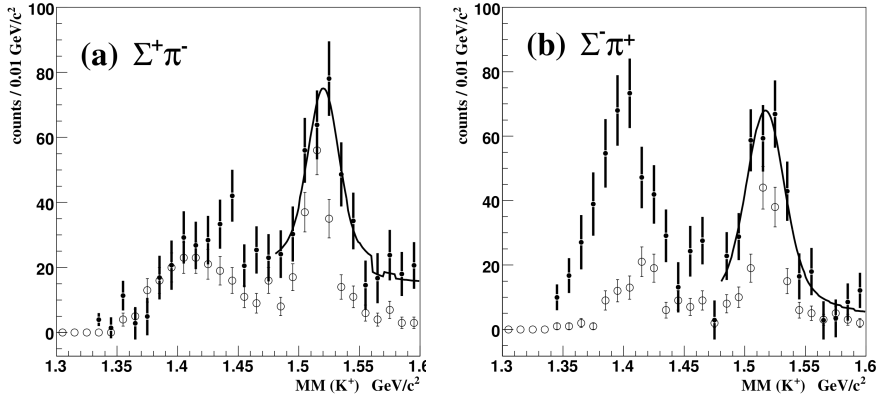
Figure 2.1: Missing mass spectrum for the $\gamma p \to K^+ X$ reaction. (a) $K^+ \Sigma^+ \pi^-$ final state. (b) $K^+ \Sigma^- \pi^+$ final state. Solid lines in the (a) and (b) frames show fits of $K^+ \Lambda(1520)$ plus nonresonant $(K^+ \pi \Sigma)$ production. Closed and open circles show spectra obtained by [1] and by the previous measurement [2], respectively.

[32] for several final states $MB = K^- p, \bar{K}^0 n, \pi^- \Sigma^+, \pi^+ \Sigma^+, \pi^0 \Sigma^0, \pi^0 \Lambda$.

2.1.2 $\Lambda(1670)$ and $\Lambda(1800)$

The $\Lambda(1670)$ and $\Lambda(1800)$ are conventionally well-established resonances that represent state with $I = 0$ isospin, $S = -1$ strangeness and $J^P = 1/2^-$. All measurements found the evidence for $\Lambda(1670)$ in the energy region 1660-1670 MeV. The width was estimated to be 25-50 MeV. The mass of $\Lambda(1800)$ was found in a range 1820-1850 MeV (beside [24]) and the width is 200-400 MeV. These properties were mostly extracted from a partial-wave analysis.

In 1977 Gopal *et al.* [33] introduced his single–channel analysis of $\bar{K}N \to \bar{K}N$ reactions using data from 1480 to 2170 MeV gathered in several experiments. A narrow S_{01} resonance at 1670 MeV and with a width 45 MeV and a broad resonance with a mass 1825 MeV and a width 230 MeV were found. Further analysis utilizing additional experimental data was given by Alston *et al.*[24]. The resonances were searched in the $\bar{K}N \to \bar{K}N$ reaction and parametrized by Breit-Wigner formula. They were in agreement with the previous analysis on $\Lambda(1670)$ but the other S_{01} resonance in their report was established at 1725 MeV with a width 175 MeV.

The partial wave analysis utilizing the reaction $K^- p \to \Sigma^\pm \pi^\mp$ was presented by Koiso *et al.* [34]. Employed data come from the measurement in Columbia–Brookhaven hydrogen bubble chamber experiment. Although this analysis had concentrated mainly on the
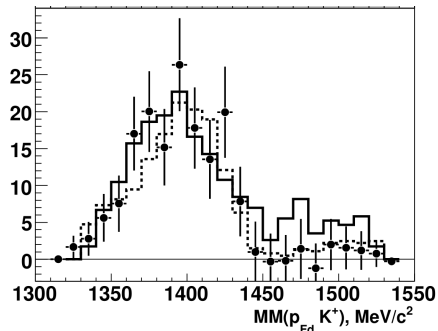
Figure 2.2: Comparison of the $\Lambda(1405)$ spectra obtained by several experiments. The solid line stands for data from the $\pi^- p \to K^0(\pi\Sigma)^0$ [3], the dotted line denotes data from $K^- p \to \pi^+\pi^-\Sigma^+\pi^-$ [4] and points denotes the spectrum for $\pi^0\Sigma^0$ final states [5]. On y-axis there are ENTRIES / 10 MeV/c^2.
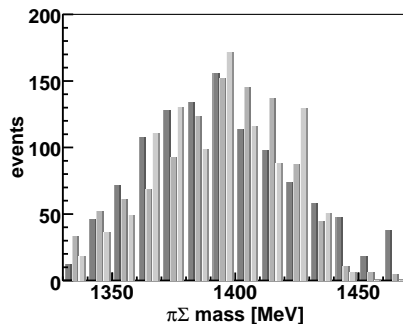
Figure 2.3: The $\pi\Sigma$ mass distribution in various experiments. Experimental data taken from Refs. [3], [4] and [5] from left to right, respectively.

$\Sigma(1660)$ resonance, the solution for the $\Lambda(1670)$ resonance was also obtained. The results are more or less in agreement with previous measurement [33] concerning the mass and width of the resonance.

A study of reactions $K^- n \to \Sigma^- \pi^0$ and $K^- n \to \Sigma^0 \pi^-$ at K^- momenta between 680 and 840 MeV/c was performed in the bubble chamber experiment at CERN. The partial wave analysis of these reactions in the center mass range from 1520 MeV to 1745 MeV was presented in [35]. They found the $\Lambda(1670)$ mass to be 1676 MeV, which was in agreement with other measurements, but the width 43 MeV turned out to be larger then the world average.

Modern experiments measured $\Lambda(1670)$ spectrum in the near-threshold reaction $K^- p \to \Lambda(1670) \to \eta\Lambda$. The results of unitary multichannel analysis, that incorporates the new Crystal Ball multiphoton spectrometer data, were reported in Ref. [36]. In this paper,

the results of the $\Lambda(1800)$ analysis were also shown. By including the [33] ([24]) elastic amplitude in their fit, a broad $\Lambda(1800)$ resonance with a mass 1845 MeV (1804 MeV) and width 518 MeV (395 MeV) was found. In their preferred fit, they obtained mass and width of $\Lambda(1670)$ to be 1673 MeV and 23 MeV. The results of $\sigma_{tot}(K^-p \to \eta\Lambda)$ are also presented in the paper. An independent analysis of $K^-p \to \eta\Lambda$ reaction was performed in Ref. [37]. There, the reaction was compared with its SU(3) flavour related partner $\pi^-p \to \eta n$ and the flavour symmetry breaking was discussed.

In addition, $\Lambda(1670)$ was observed in radiative reactions $K^-p \to \gamma\Sigma^0$ and $K^-p \to \gamma\Lambda$ in BNL Alternating Gradient Synchrotron at eight K^- momenta between 514 and 750 MeV/c [38].

In the Table 2.1, we present an overview of the $I = 0$ resonances with their observed decay channels.

Resonance	Mass[MeV]	Width[MeV]	Decay Channels
$\Lambda(1405)$	1405.1 ± 1.3	50 ± 2	$\bar{K}N, \pi\Sigma, \pi\Lambda$
$\Lambda(1670)$	$1660 - 1680$	$25 - 50$	$\pi\Sigma(25-55\%), \bar{K}N(20-30\%), \eta\Lambda(10-25\%)$
$\Lambda(1800)$	$1720 - 1850$	$200 - 400$	$\pi\Sigma(\text{seen}), \bar{K}N(25-40\%)$

Table 2.1: Overview of s-wave resonances with $S = -1$, $I = 0$ in the energy range 1300-1800 MeV from Particle data group PDG [11].

2.2 Sigma resonances

2.2.1 $\Sigma(1750)$

Sigma(1760) is a well established s-wave three stars resonance. The resonance represents a state with $S = -1$ strangeness, $I = 1$ isospin, negative parity and spin 1/2. Its decay channels are presented in Table 2.2. There is evidence for this state in many partial-wave analyses, but the problem is that various analysis give wide variations in the mass 1730-1800 MeV and in the width 60-160 MeV. The latest analyses indicate significant couplings to $\bar{K}N$ and $\pi\Lambda$, as well as to $\eta\Sigma$. According to PDG [11], the mass and width are estimated to be 1750 MeV and 90 MeV, respectively.

Energy dependent partial wave solutions for the $\pi\Lambda$, $\pi\Sigma$ and $\bar{K}N$ channels over the energy range 1480-2170 MeV were presented in Ref. [33]. The S_{11} resonance at 1770 MeV with a width 60 MeV was found in all of these channels.

In the report [24], an energy-dependent partial-wave analysis of the $\bar{K}N$ channel alone was shown. In this channel, the $\Sigma(1750)$ resonance was observed with a mass 1770 MeV and a width 161 MeV. The width obtained in this analysis is not in agreement with most of the reports reffered in PDG [11].

The latest analysis was based on the $K^-p \rightarrow \Sigma^0\eta$ reaction where the final $\Sigma\eta$ state is a pure $I = 1$ isospin state [39]. The experiment was measured in hydrogen bubble chamber in the Lawrence Berkley Laboratory. There was a bump observed in the $\Sigma\eta$ cross section spectrum. In this work, the mass and the width were determined to be 1746 MeV and 92 MeV.

2.2.2 Other Sigma resonances

There are other $I = 1$ resonances in the energy range 1300-1800 MeV, namely $\Sigma(1480)$, $\Sigma(1560)$ and $\Sigma(1620)$ resonances. However, the status of these resonances is $*$ or $**$ star resonance. In a case of $**$ star resonance, the evidence of existence is only fair. In a case of one star $*$ resonance, it means that the evidence of existence is poor. Some properties as a spin and parity are still not determined for $\Sigma(1480)$, $\Sigma(1560)$. The $\Sigma(1620)$ is a resonance with $J^P = \frac{1}{2}^-$. On the top of this only $\Sigma(1620)$ is established as an s-wave resonance. These resonances are listed in PDG mostly only tentatively in order to search for "missing" quark–model states. Thus, we do not go through experimental findings of these Sigma resonance in such detail. Despite the fact that our analysis gives also a prediction for $I = 1$ resonances in the whole energy range 1300-1800 MeV, the only one resonance with an overall status of $***$ star resonance will be compared with our theoretical predictions.

In Table 2.2, we present a brief overview of that Sigma resonance together with the $\Sigma(1750)$ resonance.

Resonance	Mass[MeV]	Width[MeV]	Out Channels
$\Sigma(1480)$	≈ 1480	$30 - 80$	$\bar{K}N, \pi\Sigma, \pi\Lambda$
$\Sigma(1560)$	≈ 1560	$15 - 80$	$\pi\Sigma, \pi\Lambda$
$\Sigma(1620)$	≈ 1620	$10 - 87$	$\bar{K}N, \pi\Sigma, \pi\Lambda$
$\Sigma(1750)$	$1730 - 1800$	$60 - 160$	$\bar{K}N(10-40\%), \pi\Sigma(seen), \pi\Lambda(<8\%), \eta\Sigma(15-55\%)$

Table 2.2: Overview of S-wave resonances with $S = -1$, $I = 1$ in the energy range 1300-1800 MeV from Particle data group PDG [11].

2.3 Theoretical studies overview

In the previous section we summarized available experimental results on the resonances with isospins $I = 0$ and $I = 1$. Although the $\Lambda(1405)$ resonance is well-established four-stars state, interpretation of its nature is a long-standing problem. Theoretical models are not able to come out with a satisfactory explanation of its peculiar features. In order to put our work into a broader perspective, we present a summary of various theoretical approaches that predict strange baryons spectra with a special accent on the $\Lambda(1405)$ resonance.

A comprehensive review article on the quark models was written by Capstick and Roberts [40]. This review focused on baryon resonances generally, not only the $\Lambda(1405)$ resonance. A recollection of various theoretical approaches dealing with the $\Lambda(1405)$ resonance was given at the beginning of a work [27].

2.3.1 Quark models

Within a quark model a systematization of hadrons with spin is based on an approximate flavor-spin symmetry $SU(6) = SU(3)_{\text{flavour}} \otimes SU(2)_{\text{spin}}$ for the six basic states is $u \uparrow$, $u \downarrow$, $d \uparrow$, $d \downarrow$, $s \uparrow$, $s \downarrow$ ($\uparrow, \downarrow =$ spin up, down) [12], [41], [42]. According to $SU(6)$, the baryons are described as three quark states and classified in (D, L_N^P) multiplets, where D is the dimensionality of the $SU(6)$ representation, L is the total quark orbital angular momentum, and P is the total parity. Concretely, the baryons are assigned to the multiplets on the right hand side of

$$6 \otimes 6 \otimes 6 = 56_S \otimes 70_M \otimes 70_M \otimes 20_A.$$

The ground states are described by the $(56, 0_0^+)$ multiplet. The negative-parity baryons with masses below about 1.9 GeV are contained in the $(70, 1_1^-)$ multiplet which decompose into $SU(3)_{\text{flavour}}$ multiplets in this way

$$70 =^2 10 \oplus^4 8 \oplus^2 8 \oplus^2 1.$$

In Tables 2.3 and 2.4, we find an assignment of observed baryons to the singlet and octet of the 70-plet. Since $\Lambda(1405)$ and $\Lambda(1520)$ have no partners in nucleon sector, they are expected to be dominantly flavor singlet states. Other resonances of our interest belong to the octet of the 70-plet. However, due to the $SU(3)$ symmetry breaking, the representations mix with each other. As a consequence, the $\Lambda(1405)$ resonance is dominantly in a singlet

configuration but includes small octet admixtures whose intensity is model dependent.

J^P	(D,L,n)	Singlet members
$1/2^-$	(1,1,1)	$\Lambda(1405)$
$3/2^-$	(1,1,1)	$\Lambda(1520)$

Table 2.3: A singlet of the 70-plet negative parity resonances [12].

J^P	(D,L,n)	Octet members			
$1/2^-$	(8,1,1)	$N(1535)$	$\Lambda(1670)$	$\Sigma(1620)$	$\Xi(?)$
$1/2^-$	(8,1,1)	$N(1650)$	$\Lambda(1800)$	$\Sigma(1750)$	$\Xi(?)$
$3/2^-$	(8,1,1)	$N(1526)$	$\Lambda(1690)$	$\Sigma(1670)$	$\Xi(1820)$
$3/2^-$	(8,1,1)	$N(1725)$	$\Lambda(?)$	$\Sigma(?)$	$\Xi(?)$
$5/2^-$	(8,1,1)	$N(1670)$	$\Lambda(1830)$	$\Sigma(1775)$	$\Xi(?)$

Table 2.4: An octet of the 70-plet negative parity resonances [12].

Let's now concentrate on factual difficulties to explain the $\Lambda(1405)$ resonance in a simple constituent quark model. The model is based on an assumption that the baryons in "soft" probe limit can be described as being made up of three constituent quarks. Such model was used by Isgur and Karl [43], [44] to calculate spectra of the negative-parity excited baryons. According to the model predictions, there are two main problems related to the $\Lambda(1405)$. Firstly, the $\Lambda(1405)$ mass is considerably lower than mass of the $N(1535)$ resonance. The problem is that the $\Lambda(1405)$ contains one strange quark and thus it should be heavier than the lowest negative parity nucleon baryon. Secondly, their model was not able to explain a large mass splitting of the $\Lambda(1405)$ and its spin–orbit partner, the $\Lambda(1520)$ resonance. In nucleon sector, the states $N(1520)$ with $J^P = (3/2)^-$ and $N(1535)$ with $J^P = (1/2)^-$ are almost degenerate in the mass while $\Lambda(1405)$ and $\Lambda(1520)$ are split by over 100 MeV. Possibly, the neglected spin-orbit interaction could split the Λ-states. These forces, which arise from one-gluon exchange, cannot be incorporated consistently into the model since they evocate unacceptably large spin-orbit splittings. A justification for ignoring the spin-orbit forces lies in a cancellation of the vector and scalar spin-orbit forces for the two-body interactions under certain conditions applied on the potentials. However there is no such cancellation for the three-body spin orbit interactions. Concerning the $\Lambda(1670)$, the mass predicted by this model almost corresponds to that observed in experiment. In a wide range of empirical resonant energies attributed to the $\Lambda(1800)$ resonance, the model predicts one state at 1800 MeV.

Corrections to the nonrelativistic model described above should be provided by a relativized quark model [45]. The later model includes one-gluon exchange and the splitting between $\Lambda(1520)$ and $\Lambda(1405)$ arises only from a spin-orbit interaction. The predicted masses of the $\Lambda(1405)$, $\Lambda(1670)$ and $\Lambda(1800)$ resonances are 1550 MeV, 1615 MeV and 1670 MeV, respectively. Here, the difference between the empirical $\Lambda(1405)$ mass and the theoretical value is caused by a presence of the nearby $\bar{K}N$ threshold.

In contrast with the Capstic and Isgur's model [45], the spin-orbit splitting without invoking the $\bar{K}N$ threshold presence was calculated by using the QCD sum rule approach [46]. In this work, the mass of the $\Lambda(1405)$ resonance was determined to be 1390 MeV whereas the $\Lambda(1520)$ mass was predicted at 1520 MeV. Simultaneously with this large splitting in Lambda sector, a small spin orbit splitting between $N(1520)$ and $N(1535)$ was obtained. The authors anticipate a possible additional shift of the $\Lambda(1405)$ mass (about 30 MeV) due to an s-wave coupling to the $\bar{K}N$ channel.

Chiral quark models describe resonances as a system of three constituent quarks that are confined by the two-body potential. Instead of assuming one-gluon exchange, the chiral quark model presume that an interaction is mediated by the $SU(3)$ octet of pseudoscalar mesons. The Goldstone boson interaction implies a reversal of ordering of the even and odd parity states between the nucleon and Lambda hyperon spectra. The analysis performed in Ref. [47] offers explanation for a large part of the $\Lambda(1405)$-$\Lambda(1520)$ splitting and predicts energies for resonances $\Lambda(1405)$, $\Lambda(1670)$ and $\Lambda(1800)$ to be 1462 MeV, 1680 MeV and 1815 MeV, respectively. The mass of the $\Sigma(1750)$ resonance was determined to be 1750 MeV.

The quark structure of resonances can also be studied by means of the $1/N_c$ expansion, where N_c is the number of colors. The analysis of the lowest negative parity 70-plet up to first order in terms of the $SU(3)$ symmetry breaking was performed in Ref. [48], [49]. Although the predictions of Ref. [48] reproduced the mass of $\Lambda(1405)$ resonance pretty well, the improved analysis of Ref. [49], that took into account the exact wave function of the component contributing to the spin term, moved the mass of the $\Lambda(1405)$ state upwards.

2.4 $\bar{K}N$ bound state and other models

Since the $\Lambda(1405)$ resonance lies only about 30 MeV under the $\bar{K}N$ threshold, alternative approach to the three quark state is a concept of an unstable meson-baryon bound state.

However, if we accepted this explanation one resonance would be missing in the multiplet classification and another state at around 1520 MeV would be required instead. Unfortunately, this sector was well explored by several $\bar{K}N$ scattering experiments with no sign of such resonance.

Phenomenological analysis [50] interprets the $\Lambda(1405)$ resonance as a virtual bound state which arises in multichannel potential from the vector meson exchange between the baryon and pseudoscalar octet. Although model predictions on the mass, width and resonant shape seem quite comparable with empirical parameters of the $\Lambda(1405)$ resonance, the authors admit that there are some inconsistencies in the way the resonance is generated in the $\pi\Sigma - \bar{K}N$ system and the vector meson exchange model is not able to give a correct dynamical explanation of the resonance and should serve only as an illustration for future models. More details can be found in [50].

The $SU(3)$ chiral extension of the cloudy bag model that describes the nucleon scattering near the threshold was performed in Refs. [51], [52] and [53]. The work of Jennings [53] extracted constraints on the model of $\Lambda(1405)$ from a phase shifts analysis of $\Lambda(1670)$ and $\Lambda(1800)$. In this approach, the $\Lambda(1405)$ resonance could in principle be either a pure quark state or a bound $\bar{K}N$ state. The low mass of the $\Lambda(1405)$ is explained as a bound state with some admixture of a three quark state (14%). Another $\Lambda(1/2)^-$ state close in mass to the $\Lambda(1520)$ is predicted in this model too.

The Skyrme model describes hyperons as bound states of kaons and skyrmeons. In the work [54], which is based on Callan–Clebanov model [55] and its vector meson generalization, the spectra of hyperon states with strangeness $S = -1$, $S = -2$ and $S = -3$ are presented. In a simplified form of the model, some exotic particles are predicted as well. Ignoring the $K - K$ interaction in this approximation results in a possibility that any number of kaons could be bound to the same skyrmeon. As the $K - K$ interactions are considered, the number of kaons K bounded to skyrmeon is limited, and that consequently determines a maximal possible value of strangeness. In this point, the skyrme model is in agreement with the quark model. Regarding the negative parity particles with $S = -1$ strangeness, the predicted state with mass 1360 MeV was assigned to $\Lambda(1405)$. Contrary to the quark model where $\Lambda(1405)$ resonance is a member of $SU(3)$ representation, $\Lambda(1405)$ has no nonstrange analogue in the skyrme model.

Another possibility is an interpretation of the $\Lambda(1405)$ resonance as a candidate of $J^P = (1/2)^-$ pentaquark [56]. The diquark picture of pentaquark predicts an octet and singlet with no orbital excitation between the diquark pair. The singlet particle with the

same quantum numbers as $\Lambda(1405)$ was predicted at 1447 MeV. In spectra of predicted states, the next Lambda particle belongs to the octet and it was predicted at 1533 MeV. Nevertheless, if the diquark picture for the pentaquark is correct, experimental observation of additional negative-parity baryons in the mass range between 1400 MeV and 1540 MeV is required.

Much effort was put into the lattice QCD investigation of the $\Lambda(1405)$ resonance. To predict the mass of the resonance, the QCD simulation with three quark operator (Ref. [57]) and five quark operator (Ref.[58]) were performed.

Chapter 3

Chiral symmetry

Although we believe to have a fundamental theory of strong interactions, the Quantum Chromodynamics (QCD), a running coupling constant causes that a different approach is required for treatment of empirical phenomena at small and large distances. Whereas the strong interaction at high energies can be handled by a perturbation theory, the low energy sector of QCD faces a problem with a large value of the strong coupling constant. Even though QCD is formulated in terms of quarks and gluons, they have never been directly observed in experiment. It seems that baryons and mesons are appropriate degrees of freedom rather than quarks and gluons at energy scale smaller than the hadron scale $\Lambda \approx 1$ GeV.

The guidance principle of the strong interactions in the low energy region is a chiral symmetry, which is the exact symmetry of QCD in the limit of vanishing quark masses. In real world, quark masses are nonzero, and thus the chiral symmetry is only approximate symmetry of QCD. This approximation works especially well at energies where one needs to consider only the lightest u and d quarks. Since the s quark mass is somewhere between light and heavy quarks masses, the extension of chiral symmetry to $SU(3)$ is still under discussion.

Spontaneous chiral symmetry breaking is connected with an existence of massless particles, the so-called Goldstone bosons. Obviously no masless particles are observed in spectra, since the chiral symmetry is not exact symmetry of QCD. The Goldstone bosons are associated with the octet of pseudoscalar mesons, which are extremely light states relatively to other particles in spectra. In addition, the spontaneous symmetry breaking puts crucial constraints on their interactions with baryons. This concept gave birth to phenomenological Lagrangians [13] and Chiral perturbation theory χPT [59]. The idea

is that one constructs the most general Lagrangian including all terms consistent with assumed symmetry. In contrast to QCD, the chiral perturbation theory expresses measurable quantities in terms of observable fields. Additionally, the chiral perturbation theory is organized as series of terms with increasing power of the energy of the particles involved in considered processes.

3.1 Phenomenological Lagrangians and Chiral Perturbation theory

In effective theory, quarks and gluons are replaced by the Goldstone boson fields and the QCD Lagrangian is replaced by an effective Lagrangian. The essential idea for construction of the phenomenological Lagrangian lies in a following rule formulated by Weinberg [13]:

One writes down the most general possible Lagrangian, including all terms consistent with assumed symmetry principles, and then calculates matrix elements with this Lagrangian to any given order of perturbation theory, the result will simply be the most general possible S-matrix consistent with analycity, perturbative unitarity, cluster decomposition and the assumed symmetry principles.

Th next important step is a systematization of chiral perturbation series, the so-called chiral power counting scheme. The series are organized in powers of derivatives on the meson fields (or equivalently in powers of small momenta), where each next term is a correction to the result. The chiral dimension D of an arbitrary Feynman diagram increases with a number of loops L and d derivatives according to

$$D = 2 + \sum_d V_d(d-2) + 2L, \tag{3.1}$$

where V_d denotes the number of vertices.

The chiral symmetry $G = SU(3)_R \times SU(3)_L$ is spontaneously broken down to a subgroup $H = SU(3)_V$. According to the Goldstone theorem, there exist eight massless Goldstone bosons connected to broken generators of the group. In real world, these states are associated with the octet of pseudoscalar mesons which are gathered in the matrix field $U(\phi) = u^2(\phi)$

$$u(\phi) = \exp\left(\frac{i\phi}{\sqrt{2}f}\right), \quad U(\phi) = \exp\left(\frac{i\sqrt{2}\phi}{f}\right) \tag{3.2}$$

with the matrix form

$$\phi = \begin{pmatrix} \frac{\pi^0}{\sqrt{2}} + \frac{\eta}{\sqrt{6}} & \pi^+ & K^+ \\ \pi^- & -\frac{\pi^0}{\sqrt{2}} + \frac{\eta}{\sqrt{6}} & K^0 \\ K^- & K^0 & \frac{-2\eta}{\sqrt{6}} \end{pmatrix}, \tag{3.3}$$

where f denotes a pseudoscalar decay constant in the chiral limit. The $u(\phi)$ field transforms nonlinearly under the global transformation

$$u(\phi) \xrightarrow{g \in G} g u(\phi) = u(\phi') h(g, u), \tag{3.4}$$

where compensator field $h(g, u)$ belongs to the subgroup H. The $U(\phi)$ representation transforms linearly under the chiral transformation

$$U(\phi) \xrightarrow{g \in G} R U(\phi) L, \quad (L, R) \in SU(3)_L \times SU(3)_R. \tag{3.5}$$

3.1.1   External sources

A systematic procedure for a calculation of amplitudes of the effective chiral Lagrangian provides a method of external sources which are generated by the functional

$$\exp[i\mathcal{Z}(v, a, s, p)] = \langle 0_{\text{out}} | 0_{\text{in}} \rangle_{v,a,s,p}. \tag{3.6}$$

Here the term on the right hand side is a vacuum-to-vacuum transition amplitude in a presence of vector (v_μ), axial vector (a_μ), scalar (s) and pseudoscalar (p) currents. The matrix elements can then be obtained by a differentiation of the functional with respect to external sources. An interaction of Goldstone bosons with external fields is described by the modified QCD Lagrangian

$$\mathcal{L}_{\text{QCD}} = \mathcal{L}_{\text{QCD}}^0 + \bar{q}\gamma^\mu(v_\mu + \gamma_5 a_\mu)q - \bar{q}(s - i\gamma_5 p)q, \tag{3.7}$$

where $\mathcal{L}_{\text{QCD}}^0$ is the QCD Lagrangian in the chiral limit $m_q \to 0$. Formally, the $\mathcal{L}_{\text{QCD}}$ is invariant under local $SU(3)_L \times SU(3)_R$

$$q(x) \to L(x)\frac{1}{2}(1 - \gamma^5)q(x) + R(x)\frac{1}{2}(1 + \gamma^5)q(x), \tag{3.8}$$

which implies a following gauge transformation of external fields

$$(s + ip) \xrightarrow{g \in G} R(s + ip)L^\dagger$$

$$l_\mu = v_\mu - a_\mu \xrightarrow{g \in G} Ll_\mu L_\dagger + iL\partial_\mu L_\dagger \tag{3.9}$$

$$r_\mu = v_\mu + a_\mu \xrightarrow{g \in G} Rr_\mu R_\dagger + iR\partial_\mu R_\dagger.$$

For a specific choice $v_\mu = a_\mu = p = 0$ and $s = \mathcal{M} = \mathrm{diag}(m_u, m_d, m_s)$ the ordinary three flavor QCD Lagrangian is recovered. The chiral Lagrangian $\mathcal{L}_{\mathrm{eff}}$ with effective degrees of freedom u is related to the QCD Lagrangian $\mathcal{L}_{\mathrm{QCD}}$ in a following way

$$\exp\left\{i\mathcal{Z}[v_\mu, a_\mu, s, p]\right\} = \int \mathcal{D}q\mathcal{D}\bar{q}\mathcal{D}A_\mu \exp i\left\{d^4x\mathcal{L}_{QCD}\right\}$$
$$= \int \mathcal{D}u \exp\left\{i \int d^4x\mathcal{L}_{\mathrm{eff}}[u, v_\mu, a_\mu, s, p]\right\}. \tag{3.10}$$

Since it is invariant under the local $SU(3)_R \times SU(3)_L$ transformation, the covariant derivatives of the meson fields $U(\phi)$ have a form

$$\nabla_\mu U = \partial_\mu U - ir_\mu U + iUl_\mu, \quad \nabla_\mu U \xrightarrow{g \in G} R\nabla UL^\dagger. \tag{3.11}$$

The scalar and pseudoscalar fields are summarized in a quantity

$$\chi = 2B_0(s + ip), \tag{3.12}$$

where B_0 is a constant related to the vacuum expectation value of the scalar quark–antiquark condensate. Consequently, we can construct the fields

$$\chi_\pm = u^\dagger \chi u^\dagger \pm u\chi^\dagger u, \tag{3.13}$$

which obey the transformation rule

$$\chi_\pm \xrightarrow{g \in G} h(g, u)\chi_\pm h^\dagger(g, u). \tag{3.14}$$

3.1.2 Meson-baryon Lagrangian

In this section, we study a coupling of mesons to baryon fields in a heavy baryon formalism and introduce resulting effective meson-baryon Lagrangian.

The octet of baryon field is given by the matrix

$$B = \begin{pmatrix} \frac{\Sigma^0}{\sqrt{2}} + \frac{\Lambda}{\sqrt{6}} & \Sigma^+ & p \\ \Sigma^- & -\frac{\Sigma^0}{\sqrt{2}} + \frac{\Lambda}{\sqrt{6}} & n \\ \Xi^- & \Xi^0 & \frac{-2\Lambda}{\sqrt{6}} . \end{pmatrix}, \tag{3.15}$$

which transforms under $g \in SU(3)_R \times SU(3)_L$ as

$$B \xrightarrow{g \in G} hBh^\dagger; \quad B \xrightarrow{g \in G} hBh^\dagger \tag{3.16}$$

with $h(g, u) \in SU(3)_V$.

In contrast to mesons, masses of the baryons do not disappear in the chiral limit and they go to a value M_0, which adds a new scale in the theory. The baryon mass M_0 has a size of a the typical hadronic scale $M_0 \approx 1$ GeV, which causes problems with the chiral power counting. These troubles can be eliminated by using an extremely nonrelativistic limit of heavy static baryon with $M_0 \to \infty$, the so-called heavy baryon perturbation theory, which was formulated by by Jenkins and Manohar [60]. To organize the perturbation series in some better way, we use the fact that a typical external momenta transfered by pions are small relatively to the baryon masses. The center of the rest mass frame is identified with the center of baryon, and thus the baryon four–momentum p_μ can be decomposed in following way

$$p_\mu = mv_\mu + l_\mu, \tag{3.17}$$

where v_μ is the baryon four-velocity (in baryon rest frame: $v_\mu = (1, 0, 0, 0)$) and l_μ denotes small residual momentum $v \cdot l \ll M_0$. The basic idea is to transfer the baryon mass from the propagator. For that purpose, the usual Dirac–spinor ψ is decomposed in velocity eigenstates by using the projection propagator $P_v = \frac{1}{2}(1 + \slashed{v})$

$$\psi(x) = \exp(-iM_0 v \cdot x)[H(x) + h(x)]$$
$$\slashed{v}H = H \qquad \slashed{v}h = -h \tag{3.18}$$

where the exponential function shifts the dependence on the baryon mass. Consequently, the large component field H obeys a modified Dirac equation $v \cdot \partial H = 0$ modulo $1/M_0$ corrections which comes from omitting the small component field h. Now, the new propagator of the H field

$$H(v \cdot k) = \frac{i}{v \cdot k + i\varepsilon}, \quad \varepsilon > 0 \tag{3.19}$$

33

has the pole in zero.

Using this approach, the leading order of effective meson-baryon Lagrangian takes a form [6]

$$
\begin{aligned}
\mathcal{L}_{\mathrm{MB}}^{(1)} =& Tr(\overline{\Psi}_B(i\gamma_\mu D^\mu - M_0)\Psi_B) + \\
& FTr(\overline{\Psi}_B\gamma_\mu\gamma_5[u^\mu, \Psi_B]) + DTr(\overline{\Psi}_B\gamma_\mu\gamma_5\{u^\mu, \Psi_B\})
\end{aligned}
\tag{3.20}
$$

with the covariant derivative of the baryon field

$$
D^\mu\Psi_B = \partial^\mu\Psi_B + \left[\frac{1}{8f^2}[\phi, \partial^\mu, \phi], \Psi_B\right] + ...,
\tag{3.21}
$$

and the axial matrix operator

$$
u^\mu = -\frac{1}{2f}\partial^\mu\phi + O(\phi^3).
\tag{3.22}
$$

The leading order $\mathcal{L}_{\mathrm{MB}}^{(1)}$ (linear in the external meson four-momentum q) includes respectively the Weinberg-Tomozawa contact term, u-channel Born term and s-channel Born term originating from the axial coupling part of $\mathcal{L}_{\mathrm{MB}}^{(1)}$. Beside that, the s-wave meson–baryon amplitudes at order $\mathcal{O}(q^2)$ and higher are generated as result of relativistic corrections to the covariant derivative term. Feynman diagrams for chiral perturbation theory up to $\mathcal{O}(q^2)$ are visualized in the Figure (3.1). The the next-to-leading order of meson–baryon Lagrangian

$$
\begin{aligned}
\mathcal{L}_{\mathrm{MB}}^{(2)} =& b_D Tr(\bar{B}\{\chi_+, B\}) + b_F Tr(\bar{B}[\chi_+, B]) + b_0 Tr(\bar{B}B)Tr(\chi_+) + \\
& d_D Tr(\bar{B}\{(u^2 + (v \cdot u)^2), B\}) + d_F Tr(\bar{B}[(u^2 + (v \cdot u)^2), B]) + \\
& d_0 Tr(\bar{B}B)Tr(u^2 + (v \cdot u)^2) + \\
& d_1 (Tr(\bar{B}u_\mu)Tr(u^\mu B)) + Tr(\bar{B}(v \cdot u))Tr((v \cdot u)B) + \\
& d_2 Tr(\bar{B}(u_\mu B u^\mu + (v \cdot u)B(v \cdot u))) + ...
\end{aligned}
\tag{3.23}
$$

gives rise to a contact term in order $\mathcal{O}(q^2)$ which is also pictured in the figure (3.1). The constants in front of the various terms in (3.23) have to be determined by fitting on the experimental data, for details see [6], [10] and the χ_+ matrix has a form

$$
\chi_+ = -\frac{1}{4f^2} = \{\phi, \{\phi, \chi\}\}.
\tag{3.24}
$$

34
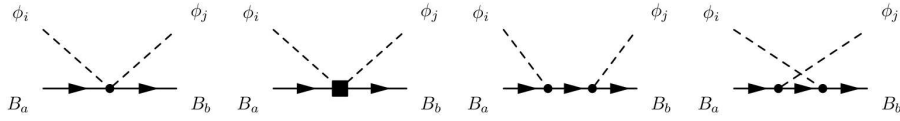
Figure 3.1: The Feynman diagrams relevant for the s-wave meson-baryon interaction. The diagrams represents from left to right $O(q^1)$ contact term, $O(q^2)$ contact term, direct s-term and crossed u-term respectively [6].

3.2 Chiral symmetry in QCD

Let's open with a brief recapitulation of quantum chromodynamics which is a non–abelian gauge theory of colored objects. The QCD Lagrangian can be written in form

$$\mathcal{L}_{QCD} = \sum_f \bar{q}_f (i\gamma^\mu \mathcal{D}_\mu - \mathcal{M}) q_f - \frac{1}{4} \mathcal{G}_{\mu\nu,a} \mathcal{G}_a^{\mu\nu} \tag{3.25}$$

with the gauge-covariant derivative

$$\mathcal{D}_\mu = \partial_\mu + ig\frac{\lambda_a}{2}\mathcal{A}_{\mu,a} \tag{3.26}$$

and the gluon field strength tensor

$$\mathcal{G}_{\mu\nu,a} = \partial_\mu \mathcal{A}_{\nu,a} - \partial_\nu \mathcal{A}_{\mu,a} - gf_{abc}\mathcal{A}_{\mu,b}\mathcal{A}_{\nu,c}. \tag{3.27}$$

Here q denotes the quark mass field, $\mathcal{M}$ stands for the diagonal mass matrix $\mathcal{M} = \text{diag}(m_u, m_d, m_s, ...)$, g is the strong coupling constant, $\mathcal{A}_{\mu,a}$ are the gluon fields which carry the color indexes $a = 1,...,8$. The structure constants f_{abc} of the $SU(3)_{\text{color}}$ Lie algebra are defined by commutation relation

$$[\lambda_a, \lambda_b] = 2if_{abc}\lambda_c, \tag{3.28}$$

where λ_a stands for Gell-Mann matrices that are linked to $SU(3)$ generators via $T_a = \frac{\lambda_a}{2}$. The non-abelian nature of quantum chromodynamics results in a gauge-field self interaction which is represented by three and four gluon vertices. On the top of this, the strong-interaction Lagrangian could also involve a anomaly (see Ref. [61])

$$\mathcal{L}_\theta = \frac{g^2\bar{\theta}}{64\pi^2}\epsilon^{\mu\nu\rho\sigma}\sum_a \mathcal{G}_{\mu\nu}^a \mathcal{G}_{\rho\sigma}^a, \tag{3.29}$$

where the $\epsilon_{\mu\nu\rho\sigma}$ is the totally antisymmetric Levi-Civita tensor. We will turn back to this term in further discussion of symmetry breaking.

Since the mass of the first three u, d and s flavour are much smaller then the typical hadronic scale $m_u, m_s, m_s << 1$ GeV, it is justifiable to examine the QCD Lagrangian in the limit of vanishing quark masses, the so-called chiral limit

$$\mathcal{L}^0_{QCD} = \bar{q}i\gamma^\mu \mathcal{D}_\mu q - \frac{1}{4}\mathcal{G}_{\mu\nu,a}\mathcal{G}^{\mu\nu}_a. \tag{3.30}$$

Let's introduce right- and left-handed quark fields

$$q_R = P_R q, \qquad q_L = P_L q \tag{3.31}$$

by defining the projection operators

$$P_R = \frac{1}{2}(1 + \gamma_5), \qquad P_L = \frac{1}{2}(1 - \gamma_5) \tag{3.32}$$

with following properties

$$P_R^2 = P_R \qquad P_R^2 = P_R \qquad P_R P_L = P_L P_R = 0 \qquad P_R + P_L = 1. \tag{3.33}$$

It is apparent that holds $q_L + q_R = q$. Using right- and left-handed quark fields we can rewrite the Lagrangian in the following way

$$\mathcal{L}^0_{QCD} = \bar{q}_R i\gamma^\mu \mathcal{D}_\mu q_R + \bar{q}_L i\gamma^\mu \mathcal{D}_\mu q_L - \frac{1}{4}\mathcal{G}_{\mu\nu,a}\mathcal{G}^{\mu\nu}_a. \tag{3.34}$$

In above, we see that quark fields decouples into the sum of two terms in which the left-handed and right-handed fields are separated fields and do not interact with each other. Therefore the Lagrangian is invariant under the chiral transformations

$$q_R = \begin{pmatrix} u_R \\ d_R \\ s_R \end{pmatrix} \longmapsto U_R \begin{pmatrix} u_R \\ d_R \\ s_R \end{pmatrix} = \exp\left(-i\Theta^R_a \frac{\lambda_a}{2}\right) \begin{pmatrix} u_R \\ d_R \\ s_R \end{pmatrix} \tag{3.35}$$

$$q_L = \begin{pmatrix} u_L \\ d_L \\ s_L \end{pmatrix} \longmapsto U_L \begin{pmatrix} u_L \\ d_L \\ s_L \end{pmatrix} = \exp\left(-i\Theta^L_a \frac{\lambda_a}{2}\right) \begin{pmatrix} u_L \\ d_L \\ s_L \end{pmatrix} \tag{3.36}$$

where U_L and U_R are unitary 3×3 matrices . In following, we debate only the part of Lagrangian $\mathcal{L}^0_{QCD}$ which is invariant under the chiral rotations.

The Noether's Theorem then implies the existence of conserved currents associated with the transformations of the left-handed quarks

$$R^\mu_a = \bar{q}_R \gamma^\mu \frac{\lambda_a}{2} q_R \qquad \text{with} \qquad \partial_\mu R^\mu_a = 0 \qquad (3.37)$$

and right-handed quarks

$$L^\mu_a = \bar{q}_L \gamma^\mu \frac{\lambda_a}{2} q_L \qquad \text{with} \qquad \partial_\mu L^\mu_a = 0. \qquad (3.38)$$

Frequently used linear combinations are quark vector currents

$$V^\mu_a = R^\mu_a + L^\mu_a = \bar{q} \gamma^\mu \frac{\lambda_a}{2} q \qquad \partial_\mu V_a = 0 \qquad (3.39)$$

and axial–vector currents

$$A^\mu_a = R^\mu_a - L^\mu_a = \bar{q} \gamma^\mu \gamma_5 \frac{\lambda_a}{2} q \qquad \partial_\mu A_a = 0. \qquad (3.40)$$

where V^μ_a and A^μ_a belongs to octet, $a = 1, .., 8$. In the limit of vanishing quark masses the Lagrangian preserves the full symmetry $SU(3)_V \times SU(3)_A \times U(1)_V \times U(1)_A$. The $U(1)_V$ symmmetry is connected to the baryon number conservation and will not be discussed in more details. Noerther's theorem implies that conserved charges can be written in form

$$Q^V_a = \int d^3 x V^a_0(x) \qquad \frac{dQ^V_a}{dt} = 0 \qquad (3.41)$$

and

$$Q^A_a = \int d^3 x A^a_0(x) \qquad \frac{dQ^V_a}{dt} = 0 \qquad (3.42)$$

which are generators of $SU(3)_V \times SU(3)_A$.

The singlet vector current $(a = 0)$

$$V^\mu = \bar{q}_R \gamma^\mu q_R + \bar{q}_L \gamma^\mu q_L = \bar{q} \gamma^\mu q \qquad \text{with} \qquad \partial_\mu V^\mu = 0 \qquad (3.43)$$

comes from a transformations of all left-handed and right-handed quark fields by the same

phase and the singlet axial-vector current

$$A^\mu = \bar{q}_R\gamma^\mu q_R - \bar{q}_L\gamma^\mu q_L = \bar{q}\gamma^\mu\gamma_5 q \tag{3.44}$$

comes from transformations of all left-handed quark fields with one phase and all right-handed with the opposite phase. The the point is that the singlet axial-vector current is not conserved on the quantum level since $U(1)_A$ symmetry is broken due to the anomaly 3.29. Furthermore, there are strong indications that even the axial vector current is not conserved in nature and thus the symmetry $SU(3)_V \times SU(3)_A \times U(1)_V$ breaks into the $SU(3)_V \times U(1)_V$. It will be discussed in more details in section 3.3.2.

3.3 Spontaneous symmetry breaking

Symmetry itself can be manifested in two possible ways, the Wigner-Weyl mode and the Nambu-Goldstone mode, which differ in the vacuum response to a symmetry transformation.

3.3.1 Symmetry realizations

The **Wigner-Weyl** mode is characterized by the symmetry realization of Lagrangian also in the ground state of the system. In this case, the symmetry is an exact symmetry of the system and generators of the symmetry acts on the vacuum state in following way

$$Q_a^A|0\rangle = 0. \tag{3.45}$$

If we take into account the commutation relation of the Hamiltonian of the system with the symmetry generators

$$[H, Q_a^A] = 0, \tag{3.46}$$

we get a degeneracy of states in multiplets. Let's consider for example two energy eigenstates of the same multiplet denoted $|a\rangle$ and $|b\rangle$, such that $|b\rangle = Q_a^A|a\rangle$. If we apply the commutation relation on $H|a\rangle = E_a|a\rangle$, we simply get $H|b\rangle = E_a|b\rangle$ which symbolize that the $|a\rangle$ and $|b\rangle$ states are degenerate in energies.

In the **Goldstone mode**, which is also called a spontaneous symmetry breaking, the ground state of the system is no longer invariant under the full symmetry group of the

Lagrangian

$$Q^A|0\rangle \neq 0 \tag{3.47}$$

for number of generators. It is said that the symmetry is spontaneously broken.

According to **Goldstone theorem**, the spontaneous symmetry breaking is connected with existence of massless mode - the Nambu–Goldstone (NG) bosons coupled to the axial currents $A_a^\mu(x)$ with quantum numbers of the broken generators. The number of Goldstone bosons is given by the number of broken generators.

3.3.2 Evidence of spontaneous symmetry breaking

In real world, there is a few indications that the symmetry is realized in the Nambu–Goldstone mode. If the chiral symmetry was the exact symmetry of QCD, the symmetry of Lagrangian would naturally lead to symmetry of states. As the degenerancy in charge of particles in spectra $SU(3)_V$ (isospin symmetry) is observed, one would expect same degenerancy between hadron multiplets of opposite parity $SU(3)_A$ (axial–vector symmetry). To each a degenerate hadron state of positive parity should exist a negative parity hadron and vice versa. In reality, these parity doublets are not observed since the meson mass spectrum does not respect the axial–vector symmetry. The hadron spectra is visualized in the figure 3.2. One can see the splitting of the positive (negative) parity ground states and the first negative (positive) parity states. The situation described above causes spontaneous breaking of the $SU(3)_V \times SU(3)_A \times U(1)_V$ symmetry down to the $SU(3)_V \times U(1)_V$ symmetry.

Now, as we know that symmetry is spontaneously broken, we naturally ask for some massless Nambu-Goldstone boson candidate. The (NG) bosons are identified with the lightest pseudoscalar mesons (π, K and η) and their small but nonzero mass arises due to an explicit symmetry breaking which is consequence of the nonvanishing quark masses.

According to QCD foundations the spontaneous symmetry breaking is induced by a non-vanishing value of a singlet scalar quark condensate

$$\langle 0|\bar{q}q|0\rangle = \langle 0|\bar{q}_R q_L + \bar{q}_L q_R|0\rangle, \tag{3.48}$$

which it is not invariant under the chiral transformations due to the mixing the left- and right-handed quarks operators. On the contrary, the $SU(3)_V$ rotates the left- and right-handed simultaneously. Since the finite expectation value of the scalar quark condensate should be melt away in high temperatures and densities, the chiral symmetry restoration
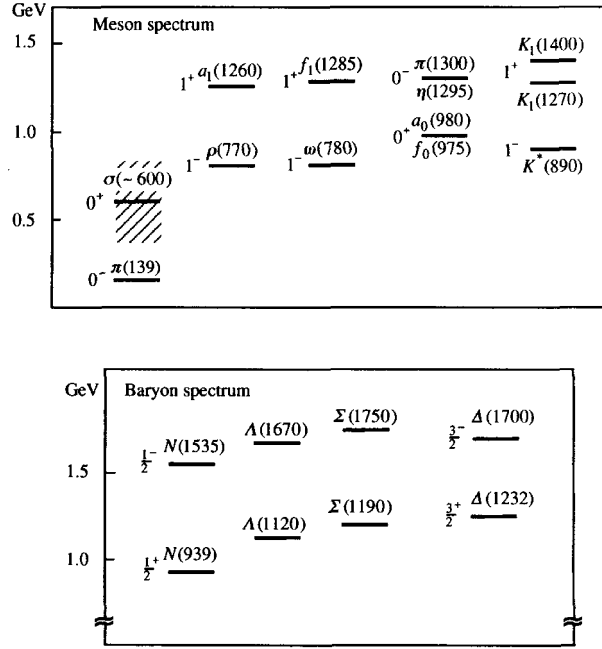
Figure 3.2: Masses of mesons and baryons of opposite parity [62].

is expected. The symmetry then would be realized in the Wigner-Weyl mode.

3.3.3 Low energy theorems

As was already said, the spontaneous symmetry breaking is connected to non-conservation of the axial current. This can be demonstrated by weak pion decay which is a pure axial-isovector transition. The matrix element of the axial-vector current operator between the vacuum and the NG-boson state can be written as

$$\langle 0|A_a^\mu(x)|\pi_a(p)\rangle = -if_\pi p^\mu e^{-ip\cdot x}\delta_{ab}, \tag{3.49}$$

where a and b are isospin indices and p^μ denotes four momentum. Above equation defines the pion decay constant f_π which can be deduced from the accurately measured lifetime of the charged pions

$$f_\pi \cong 93 \text{ MeV}. \tag{3.50}$$

The divergence $\partial_\mu A^\mu$ of the axial current then gives

$$\langle 0|\partial_\mu A_a^\mu(x)|\pi_a(p)\rangle = -if_\pi p^2 e^{-ip\cdot x}\delta_{ab}. = -if_\pi m_\pi^2 e^{-ip\cdot x}\delta_{ab} \tag{3.51}$$

40

If the axial current was exactly conserved, it would imply

$$f_\pi m_\pi^2 = 0. \tag{3.52}$$

Since the pion mass is nonzero but small compared to hadronic scales, the axial current is approximately conserved.

The above relations lead to identification of the axial-vector current divergence with the pion field

$$A_{\mu,\text{pion}}^a = f_\pi \partial_\pi \Phi^a(x), \tag{3.53}$$

where $\Phi^a(x)$ is the pion field. Sometimes the relation between pion field and axial current is referred to as the partially conserved axial vector current (PCAC) relation. Apparently, such a relation can serve as justification of the chiral symmetry concept for treating low energy dynamics of the NG boson and simultaneously supports the usage of mesons and baryons as a relevant degrees of freedom in chiral perturbation theory instead of quarks and gluons which are the fundamental building blocks of QCD.

3.4 Explicit symmetry breaking

Even though the existence of the Goldstone bosons was attributed to spontaneous symmetry breaking, to explain its small nonzero mass is necessary to take into account the explicit symmetry breaking. The chiral symmetry is not an exact symmetry of the strong interactions any more. If we consider the finite current quark masses, the mass term $-\bar{q}\mathcal{M}q$ in the QCD Lagrangian Eq. 3.25 breaks chiral symmetry explicitly

$$\mathcal{M} = \begin{pmatrix} m_u & 0 & 0 \\ 0 & m_d & 0 \\ 0 & 0 & m_s \end{pmatrix}. \tag{3.54}$$

If we substitute the left-handed and right-handed quark field into into quark mass term, we see that the left and right components are mixed in the Lagrangian

$$\mathcal{L}_M = -\bar{q}Mq = -(\bar{q}_R M q_L + \bar{q}_L M q_R). \tag{3.55}$$

Since the masses of u, d and s quarks are small compared to the typical hadronic scale, the explicit chiral symmetry breaking due to the non-vanishing quark masses is very small.

Inclusion of the mass term into the Lagrangian cause additional divergences of vector and axial-vector currents. However, the flavour currents $\bar{u}\gamma^\mu u$, $\bar{d}\gamma^\mu d$ and $\bar{s}\gamma^\mu s$ are always conserved for any quark mass value which indicates the flavour independency of strong interaction and the diagonality of the quark mass matrix [61]. As consequence, the singlet vector current V^μ which is a sum of the three flavours, is conserved.

Chapter 4

Coupled channel approach

The previous chapter was devoted to the effective chiral Lagrangians and the chiral perturbation theory. However, problems with chiral series arise as we go to higher orders in a perturbative expansion. In $SU(3)$ sector, the perturbation series fails due to the presence of the $\Lambda(1405)$ resonance just below the $\bar{K}N$ threshold. This problem can be addressed by a nonperturbative technique witch is based on a solution of scattering equation in a coupled channel formalism. For this purpose, we employ a Lippman-Schwinger equation with entering meson–baryon potential in a separable form. This interaction potential is derived from the chiral perturbation theory as an effective transition amplitude which gives a same scattering length as that we get from the effective Lagrangian in a calculation up to a given order in external meson momenta. Dynamically generated resonances arises as a consequence of the multiple scattering in the interaction of the pseudoscalar meson octet $(\pi, K, \bar{K}, \eta)$ with the baryon octet $(N, \Lambda, \Sigma, \Xi)$.

4.1 Effective meson-baryon potentials

In our model, the potential matrix describing a coupling of the pseudoscalar meson octet with the baryon octet is taken in a separable form

$$V_{ij}(k_i, k_j) = \sqrt{\frac{1}{2E_i}\frac{M_i}{\omega_i}}\, g_i(k_i)\frac{C_{ij}}{f^2}g_j(k_j)\sqrt{\frac{1}{2E_j}\frac{M_j}{\omega_j}} \tag{4.1}$$

with the off-shell Yamaguchi form factors

$$g_i(k_i) = \frac{1}{1 + (\frac{k_i}{\alpha_i})^2}, \tag{4.2}$$

where inverse range radii α_i characterize the range of interaction in channel i and k_i denotes momentum in the meson–baryon c.m. frame. The symbols E_i, M_i and ω_i denote meson energy, baryon mass and baryon energy the in the c.m. frame, respectively, and f stands for the pseudoscalar meson decay constant.

The chiral $SU(3)$ symmetry is reflected in a structure of the C_{ij} coupling coefficients which are derived directly from the effective chiral Lagrangian.

The Lippman-Schwinger equation for transition amplitude T between coupled channels in operating form reads

$$T = V + VGT, \tag{4.3}$$

where G denotes the two body Green function. Substituting the whole right hand side into the T operator in the right hand side successively we obtain an infinite sum of multiple meson-baryon scattering. Corresponding integral equation is given in a form

$$T_{ij}(k_i, k_j) = V_{ij}(k_i, k_j) + \sum_{n=1}^{N} \frac{\mu_n}{2\pi} \int d^3 l \frac{V_{in}(k_i, l) T_{nj}(l, k_j)}{k_n^2 - l^2 + i\varepsilon}, \tag{4.4}$$

where the meson-baryon reduced mass is $\mu_i = E_i\omega_i/(E_i + \omega_i)$, k_n denotes the off-shell meson-baryon relative momenta in intermediate channel n and N is the total number of considered outgoing channels. In this work, we are interested in baryon resonances with the strangeness $S = -1$ and charge $Q = 0$, that appears in elementary reaction of the K^-p interaction. The possible outgoing channels are: $\pi^0\Lambda$, $\pi^0\Sigma^0$, $\pi^-\Sigma^+$, $\pi^+\Sigma^-$, K^-p, $\bar{K}^0 n$, $\eta\Lambda$, $\eta\Sigma^0$, $K^0\Xi^0$, $K^+\Xi^-$.

The solution of the integral equation (4.4) should incorporate a resummation of the expanded scattering amplitude. Through the using potential in separable form

$$v_{ij}(k, k', \sqrt{s}) = (-\mu_{ij}/2\pi)V_{ij}(k, k', \sqrt{s}) = g_i(k^2)v_{ij}(\sqrt{s})g_j(k'^2) \tag{4.5}$$

we get the elementary s-wave amplitudes in separable form

$$t_{ij}(k, k', \sqrt{s}) = (-\mu_{ij}/2\pi)T_{ij}(k, k', \sqrt{s}) = g_i(k^2)t_{ij}(\sqrt{s})g_j(k'^2) \tag{4.6}$$

44

we get the variables v_{ij} and t_{ij} independent of momenta, and thus they can be factored out from momentum integration of equation (4.4). The symbol μ_{ij} stands for $\sqrt{\mu_i \mu_j}$ and $\sqrt{s} = E_i + \omega_i$ is center mass energy.

This allows to reduce the integral equation to algebraic equation

$$t_{ij} = v_{ij} + \sum_{n=1}^{N} v_{in} G_n t_{nj} \tag{4.7}$$

whereas the momentum integration of Green function G_n can be performed separately

$$G_n = 2\mu_n \int_{\Omega_i(p_F)} \frac{d^3 l}{(2\pi)^3} \frac{g_n(l)^2}{k_n^2 - l^2 + i\varepsilon} = -\frac{\mu_n}{2\pi} \frac{(\alpha_n + ik_n)^2}{2\alpha_n} g^2(k_n). \tag{4.8}$$

Consequently, the solution of the algebraic Lippman-Schwinger equation (4.7) can be given in matrix form

$$t = (v^{-1} - G)^{-1} \tag{4.9}$$

and resonances are then searched as poles of T-matrix

$$\det|t^{-1}| = \det|v^{-1} - G| \tag{4.10}$$

in the complex energy plane, mainly on the second Riemann sheet. The z is equal to the meson-baryon cms energy $\sqrt{s}$ at the real axis.

4.2 $\bar{K}N$ data fits

Potential model described above includes few free parameters which have to be fitted to available experimental data. Our calculations are done with three models called TW1 [10], CS30 [6] and NLO30 [10], that differ mainly in fitted parameters and in the order of the effective chiral Lagrangian.

The free parameters of the models are:

- Parameters of first and second order of the Lagrangian entering into the C_{ij} coupling matrix (D, F, d_0, d_1, d_2, b_0, b_D, b_F, d_D, d_F).

- Five inverse range radii α_{KN}, $\alpha_{\pi\Lambda}$, $\alpha_{\pi\Sigma}$, $\alpha_{\eta\Lambda/\Sigma}$, $\alpha_{K\Xi}$.

- The pseudoscalar meson-decay constant f.

- The ratio $r_{KN/\pi\Sigma}$ of a relative coupling of the $\Lambda(1405)$ resonance to the KN and the $\pi\Sigma$ channels.

Some parameters of the Lagrangian were determined prior to performing the fits. The D and F couplings were fixed in analysis of semileptonic decays, the b_D and b_F constants were set to satisfy the approximate Gell–Mann formulas for the baryon mass splitting

$$
\begin{aligned}
M_\Xi - M_N &= -8b_F(m_K^2 - m_\pi^2) \\
M_\Sigma - M_\Lambda &= \frac{16}{3}b_D(m_K^2 - m_\pi^2),
\end{aligned}
\tag{4.11}
$$

and finally the b_0 coupling was fixed such that we get a value of the pion nucleon sigma term $\sigma_{\pi N} = 30$ MeV.

$$
\sigma_{\pi N} = -2m_\pi^2(2b_0 + b_D + b_F).
\tag{4.12}
$$

In the CS30 and NLO30 models, the leading (LO) plus next-to-leading (NLO) order correction of the chiral Lagrangian are considered, thus the remaining free parameters of these models are: the low energy constants d_0, d_1, d_2, d_D, d_F from the second order chiral Lagrangian, five inverse range radii α_{KN}, $\alpha_{\pi\Lambda}$, $\alpha_{\pi\Sigma}$, $\alpha_{\eta\Lambda/\Sigma}$, $\alpha_{K\Xi}$, the meson-baryon chiral coupling f and the ratio $r_{KN/\pi\Sigma}$. The numeral 30 in names of the CS30 and NLO30 models signifies that it was used the pion nucleon sigma term $\sigma_{\pi N} = 30$ MeV.

In practice, one often considers only the leading order Weinberg-Tomozawa (WT) interaction with energy dependence given by

$$
C_{ij} = -C_{ij}^{(WT)}(2\sqrt{s} - M_i - M_j)/4,
\tag{4.13}
$$

where C_{ij}^{TW} denotes $SU(3)$ Clebsh-Gordan coefficients. The details of the C_{ij} energy dependence as well as their exact content of matrix elements are listed in Refs. [6],[10]. The simplest is the TW1 model because takes into account only the leading order WT interaction and consequently we do not need to consider free parameters d_0, d_1, d_2, d_D, d_F in this model.

Since the parameters α_i characterize inverse ranges of meson-baryon interaction, their values have to be constrained by a mass of the lightest exchanged particle, the pion. Another restrictions prevent from unphysical resonances emerging as poles for $\alpha_i^2 + k^2 = 0$ in the off-shell form factors. In case of the TW1 model, only one inverse range parameter common to all channels was used and one average meson decay constant was considered.

On the other hand, the CS30 and NLO30 model used various inverse range parameters in each channel α_{KN}, $\alpha_{\pi\Lambda}$, $\alpha_{\pi\Sigma}$, $\alpha_{\eta\Lambda/\Sigma}$, $\alpha_{K\Xi}$. Inspired by the idea of Ref.[63], physical values of the meson decay constants f_π, f_K and f_η was adopted in the NLO30 model. For details see [6],[10].

The value of $r_{KN}/\pi\Sigma$ parameter is adjusted in a way that the fits are performed using selected experimental data first and then the position of $\Lambda(1405)$ peak is fixed.

The available experimental data on low energy $\bar{K}N$ interaction includes:

- Kaonic hydrogen 1s level shift and width (performed by DEAR [64] or SIDDHARTA [65] experiment).

- Threshold branching ratios γ, R_c, R_n [66]

- K^-p cross sections (same as those compiled in Ref. [22]).

Important constraints on the theoretical models are provided by the measurement of the K-series x rays of kaonic hydrogen. Despite the fact that some unreliable old experiments generated the attractive energy shift, new improved experiments confirmed the repulsive interaction which is in agreement with other low energy $\bar{K}N$ scattering data. The first experiment that reported repulsive energy shift was the KEK measurement [67], [68]. However, the statistics of the KEK experiment was insufficient and nowadays more precise data on the kaonic hydrogen are available.

The DEAR experiment [64] obtained the energy of x rays emitted in the transitions to the ground state of kaonic hydrogen with the uncertainty about 2 times smaller than that of the KEK values. The resulting 1s-level shift ϵ_{1s} and width Γ_{1s} of kaonic hydrogen were determined to be

$$\epsilon_{1s} = -193 \pm 37(\text{stat}) \pm 6(\text{syst}) \text{ eV}$$
$$\Gamma_{1s} = 249 \pm 111(\text{stat}) \pm 30(\text{syst}) \text{ eV}. \tag{4.14}$$

Recently, the SIDDHARTA colaboration introduced the most precise values of the strong-interaction energy-level shift and width of the 1s atomic state [65]. The signal-to-background ratio was improved by a factor more than 10 compared to the DEAR experiment. The resulting ground-state 1s-energy level shift and the strong interaction width

are

$$\epsilon_{1s} = -283 \pm 36(\text{stat}) \pm 6(\text{syst}) \text{ eV}$$
$$\Gamma_{1s} = 541 \pm 89(\text{stat}) \pm 22(\text{syst}) \text{ eV}. \tag{4.15}$$

The measurement of branching ratios (Ref. [66]) is old but very precise and gives good constraints on model parameters

$$\gamma = \frac{\sigma(K^-p \to \pi^+\Sigma^-)}{\sigma(K^-p \to \pi^-\Sigma^+)} = 2.36 \pm 0.04$$
$$R_c = \frac{\sigma(K^-p \to \pi^+\Sigma^-, \pi^-\Sigma^+)}{\sigma(K^-p \to \text{all inelastic channel})} = 0.664 \pm 0.011 \tag{4.16}$$
$$R_n = \frac{\sigma(K^-p \to \pi^0\Lambda)}{\sigma(K^-p \to \text{all neutral states})} = 0.189 \pm 0.015.$$

For fits of the K^-p cross section were considered the data points at the kaon laboratory momenta $p_{\text{LAB}} = 110$ MeV (for the K^-p, $\bar{K}^0n$, $\pi^+\Sigma^-$, $\pi^-\Sigma^+$ final states) and at $p_{\text{LAB}} = 200$ MeV (for the same four channels plus $\pi^0\Lambda$ and $\pi^0\Sigma^0$) Obtained fits can be found in [6].

4.2.1 Variants of chirally motivated models

Before we introduce our predictions for the dynamically generated $S = -1$ resonances, we would like to give an overview of other chirally motivated models that are relevant for a comparison with our predictions. Contrary to our approach, all models presented below are based on manifestly Lorentz invariant formulation of chiral Lagrangian that differs from heavy baryon formalism described in section 3.1.2. Our approach is based on solution of Lippman–Schwinger equation with effective potential. The off-shell form factors added to the separable potential are parametrized by means of the inverse range radii, which play a role of natural cut-offs on the range of interactions. However, there is more variants of treating the scattering amplitude by ensuring its unitarity.

Other approaches are based on quantum field techniques such as the N/D scheme, unitarity relation for the inverse of the T-matrix and on the dimensional regularization of the intermediate state wave function in which momenta are considered only on-shell. The have advantage of using a completely relativistic dynamics. Nevertheless in those approached, an employment of additional subtraction constants in a renormalization procedure is required. Moreover, the quantum field approach is not necessary at low and

medium energies.

In Table 4.1 we compare our TW1, NLO30 and CS30 models with other selected theoretical models BNW [21], JOORM [7] and IHW [8] in terms of their ability to reproduce $\bar{K}N$. For future reference, we also show the position of poles z_1 and z_2 assigned to the $\Lambda(1405)$ resonance The first two lines include models incorporating only Weinberg–Tomozawa interaction and the remaining two lines present models which implement LO plus NLO terms. Comparison with experimental data can be obtained from the last two lines. It's obvious that satisfactory reproduction of the threshold data are provided already by the models using only on the TW interaction.

All models BNW [21], JOORM [7] and IHW [8] we compare with, are based on the on-shell methods mentioned above. The model use kaonic hydrogen data that were available at the time of their publication. The KEK experimental data [67], [68] were used in the JOORM [7] but the branching ratios R_c, R_n and γ are not reproduced well. The BNW model incorporates the data from kaonic measurement at DEAR experiment [64] and the IHW model uses most recent data from SIDDHARTA measurement [65].

model	ΔE_{1s}	Γ_{1s}	γ	R_c	R_n	z_1	z_2
TW1	323	659	2.36	0.636	0.183	$1371 - 54i$	$1433 - 25i$
JOORM [7]	275	586	2.30	0.618	0.257	$1389 - 64i$	$1427 - 17i$
NLO30	310	607	2.37	0.660	0.191	$1355 - 86i$	$1418 - 44i$
CS30	260	692	2.37	0.655	0.188	$1398 - 51i$	$1441 - 76i$
BNW [21]	236	580	2.35	0.653	0.194	$1408 - 37i$	$1449 - 106i$
IHW [8], [9]	306	591	2.37	0.66	0.19	$1381 - 81i$	$1424 - 26i$
exp.	283	541	2.36	0.664	0.189	–	–
error($\pm$)	42	111	0.04	0.011	0.015	–	–

Table 4.1: K^-p threshold data calculated in several LO and LO+NLO coupled-channel chiral models. The columns show the kaonic hydrogen 1s level shift ΔE_{1s} and width Γ_{1s} (in eV), and the K^-p threshold branching ratios γ, R_c , R_n . The last two columns list the $I = 0$ S-matrix pole positions z1 , z2 (in MeV) related to the $\Lambda(1405)$ resonance. The last two lines show the experimental data and their errors [10].

Chapter 5

Pole analysis

The technique for a construction of the transition amplitude in coupled channel approach was formulated in previous chapter. Here we show analysis of the scattering amplitude as an analytic function of complex variables and how the singularities of the amplitude on specific Riemann sheet are related with resonances and bound states. We present the pole content of our chiral models TW1 [10], NLO30 [10] and CS30 [6] in a range of energies 1300-1800 MeV. Afterwards, we match our results with experimentally measured resonances reported in PDG [11] and with predictions of other chirally motivated models which were discussed in section 4.2.1. Furthermore, we are trying to learn more about the origin of the poles. This is achieved by following the pole movements on the complex energy manifold into the zero coupling limit and to the $SU(3)$ symmetry limit. We recall that our work is focused on s-wave strange $S = -1$ resonance with the $I = 0$ and $I = 1$ isospins.

5.1   Poles on Riemann sheets

In following, we clarify how the location of poles in the complex energy plane on various Riemann sheets gives an information about the related physics (for details see Ref. [69]). We give a brief introduction into the classification of such singularities and Riemann sheets on which they residue.

Since we deal with multichannel problem containing 10 meson-baryon decay channels ($\pi^0\Lambda$ $\pi^+\Sigma^-$, $\pi^0\Sigma^0$, $\pi^-\Sigma^+$, K^-p, $\bar{K}^0n$, $\eta\Lambda$, $\eta\Sigma^0$, $K^0\Xi^0$ and $K^+\Xi^-$) arising from K^-p interaction, we examine the transition matrix which is, by analytic continuation, a function of momentum in these channels.

To explain basic ideas of the collision theory, we restrict ourselves for the moment to a one channel problem. In this case, we distinguish physical Riemann sheet which is defined by the positive value of the imaginary part of the c.m. meson baryon momenta Im $q > 0$ and unphysical Riemann sheet for which imaginary part of the c.m. momenta is negative Im $q < 0$. For our purposes, its more convenient to treat the the scattering amplitude in terms of energy rather then momentum. Since the momentum is a double valued function of energy, the mapping from the complex momentum plane to the energy momentum plane is two-to-one, as it is visualized in Figure 5.2. The upper half momentum plane maps onto the physical energy sheet (phase range $0 \leq \phi_E \leq 2\pi$) with a cut along the positive real axis from the branching point at $E = 0$. The lower half momentum plane corresponds to a continuation through the cut to phase range a $2\pi \leq \phi_E \leq 4\pi$.

Let's have a look at the type of singularities that can be found on specific Riemann sheets in a more detail. The physical sheet, sketched in the picture 5.1, accommodates the poles confined to the imaginary axis on complex momentum plane, respectively to negative real axis below the $E = 0$ on complex energy plane. These poles represent bound states.
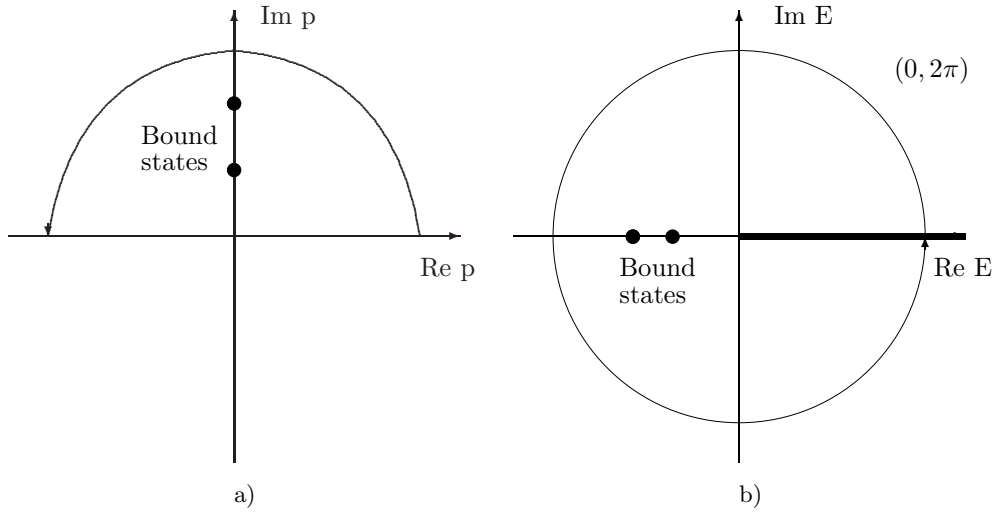
Figure 5.1: Singularity classification on the physical Riemann sheet in the one channel case. Correspondence of the momentum complex plane a) to energy plane with b). The line on the real axis denotes the branch cut from $E = 0$ to infinity. Full circles visualize bound states.

A possible situation on the unphysical sheet is schematically visualized in the Figure 5.2. On the complex energy plane we find poles below the real axis that are related with resonances. To estimate the energy of the resonance E_R in the c.m. meson-baryon system
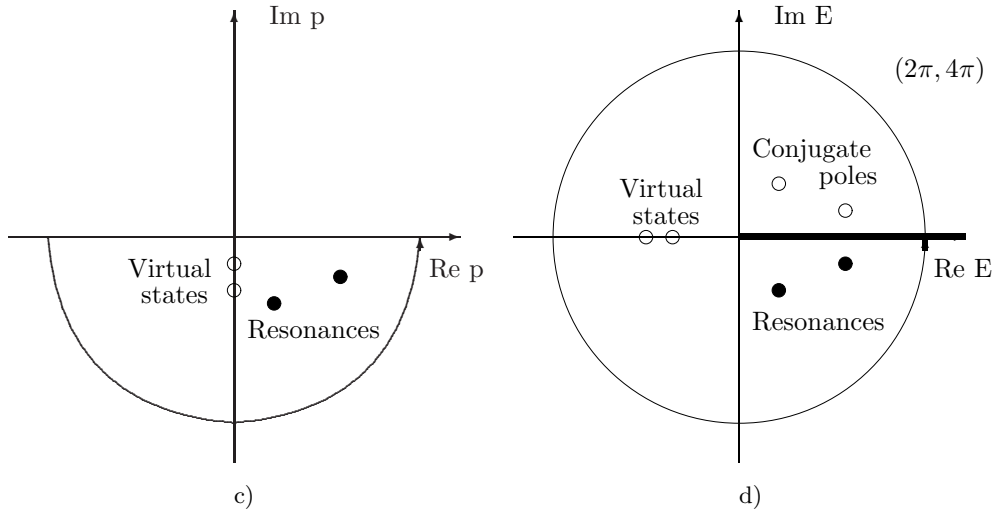
Figure 5.2: Singularity classification on the unphysical Riemann sheet in the one channel case. Correspondence of the momentum complex plane c) to energy plane with d). The line on the real axis denotes the cut from $E = 0$ to infinity. Open circles on imaginary axis in momentum plane and on real axis in energy plane denote virtual states. Full circles visualize resonant poles at energy and open circles denotes the conjugate poles.

and resonant width Γ we can use of an approximate relation for the pole position z in the complex energy plane

$$\bar{z} \approx E_R - i\frac{\Gamma_R}{2}, \tag{5.1}$$

which is valid chiefly near by the real axis. The authors of Ref. [70] showed, that each resonant pole is accompanied by its conjugate pole situated on the upper half energy plane symmetrically to the real axis at complex conjugate energy E_R^*. The poles on real axis referred to as virtual states (sometimes also called quasi–bound states) are not proper bound states. They appear if scattering potential is slightly less attractive to create a bound state, see the Ref. [69] for more details.

If we consider multichannel case, we get a sequence of thresholds where at each threshold a new channel opens up. The Riemann surface is now more complicated and composed of several Riemann sheets which are connected together through additional branch cuts associated with the energy threshold. The notation of the Riemann sheets is following. Each Riemann sheet is marked by a string of signs, where the signs are those of the imaginary parts of the c.m. momenta in the meson–baryon channels ordered according to their threshold energies. Among the Riemann sheets, there exist one unique Riemann sheet, the physical sheet in which all channel momenta are positive. For our 10 channels

sheet is marked $[+ + + + + + + + + +]$. Then there is N unphysical sheets that can be reached directly from the physical sheet. Total number of sheets in ten channel problem is 2^{10}.

To explain linking of Riemann sheets, let's us take an example the unphysical $[- - - - + + + + + +]$ sheet, which is is characterized by negative momenta in the first $\pi^0\Lambda$, $\pi^0\Sigma^0$, $\pi^-\Sigma^+$, $\pi^+\Sigma^-$ channels and the imaginary part of momenta in remaining K^-p, $\bar{K}^0n$, $\eta\Lambda$, $\eta\Sigma^0$, $K^0\Xi^0$, $K^+\Xi^-$ channels are positive. This sheet is connected to the physical sheet by crossing the real axis between the thresholds of the $\pi^+\Sigma^-$ and K^-p channels.

In multichannel case, a pole may occur on the real axis above some energy threshold. However, the pole must always lie below the threshold of channel in which is observed. If we observe such pole on the real axis on the Riemann sheet which is physical in the appropriate channel, then the pole corresponds to a bound state and if the pole is observed on the Riemann sheet which is unphysical in the appropriate channel, then the pole is is referred to as a quasi-bound state.

On more distant Riemann sheets, there are shadow poles related to the resonant pole [71]. Once the pole is on Riemann sheet that is not directly connected with the physical region, the length of trajectory path of pole to the physical sheet is important. The physical sheet represents the physical reality. It can be said that the nearer the poles are to the physical Riemann sheet, the closer they are to a physical reality and have a larger effect on physical observables. The definition of the shadow poles is not so straightforward. As the parameters of the model are varied, the poles move on the complex energy manifold. Eventually, the shadow and the resonant pole may get to the position where one cannot distinguish between them or even the shadow pole may lie at the position closer to the physical sheet than the resonant poles. In this case, the shadow pole takes over the role of a resonant pole.

To determine the isospin of a resonance we incorporate an isoscalar or isovector base in which we consider only $\pi\Sigma$, $\bar{K}N$, $\eta\Lambda$, $K\Xi$ channels or $\pi\Lambda$, $\pi\Sigma$, $\bar{K}N$, $\eta\Sigma$ and $K\Xi$ channels, respectively. In isoscalar base, one finds only isoskalar poles, isovector poles disappears and vice versa. The principle lies in coupling the Clebsh–Gordan coefficients together so that we obtain pure isoscalar (isovector) states. These isoskalar (isovector) coefficients for Weinberg-Tomozawa model are listed in paper [23] together with the NLO coefficients for the 10 channel base. The general transformation relations between the physical and isoscalar (isosvector) Clebsh–Gorgan coefficients was determined by a decomposition of $I = 0$ $(I = 1)$ transition amplitudes into pertinent physical channels. These relations, which

are referred in Appendix, can be used for a calculation of the NLO isoscalar (isovector) coefficients.

5.2   Identification of poles with resonances

In this section, we explore the pole content of our chiral models TW1, NLO30 and CS30 and classify the poles according to the mass, width and isospin. The overview of all isoscalar and isovector pole positions and the Riemann sheets on which they are situated, is given in Tables 5.1 and 5.2, respectively. Their correspondence to the experimentally observed resonances is suggested there too. Our results are commented in more detail in the text below.

5.2.1 $\Lambda(1405)$

We start our discussion with the two z_1 and z_2 isoscalar poles related to the $\Lambda(1405)$ resonance. In chirally motivated models, the $\Lambda(1405)$ spectrum is assumed to be a super-position of these two dynamically generated states, found in $\pi\Sigma$ and $\bar{K}N$ amplitudes on the unphysical $[-+++]$ Riemann sheet which is achieved by crossing the real axis between the $\pi\Sigma$ and $\bar{K}N$ energy thresholds. Typically, the lower (in terms of Re z) pole z_1 has quite large imaginary part which indicates a large resonant width. This fact results in a rise of the background rather than observation of significant experimental peak. The position of the higher pole z_2 is more likely associated with the observed $\pi\Sigma$ mass spectrum in the $\bar{K}N$ initiated reactions.

The situation for poles of the $\Lambda(1405)$ resonance outlined above was observed for our recent TW1 and NLO30 models. On the contrary, the CS30 model generates the z_1 pole closer to the real axis than the z_2 pole, as can be seen in Figure 5.3. In this figure, we present in comparison the positions of the isoscalar poles as provided by various models. The position of the pole z_2 at higher energies is more or less stable in all Weinberg-Tomozawa (WT) models and does not depend much on a choice of the parameter set. Our recent TW1 model generates the pole at the position $z_2 = 1433 - i25$ MeV. This result would correspond preferably to the narrow peak of the $\Lambda(1405)$ resonance with the width about 50 MeV referred in PDG [11]. We also note that all WT models [7], [8], [9] generate the z_2 pole at very similar positions.

On the other hand the z_1 pole position is quite model dependent even in the LO order of calculation. However, since it imaginary part is large it should not substantially affect
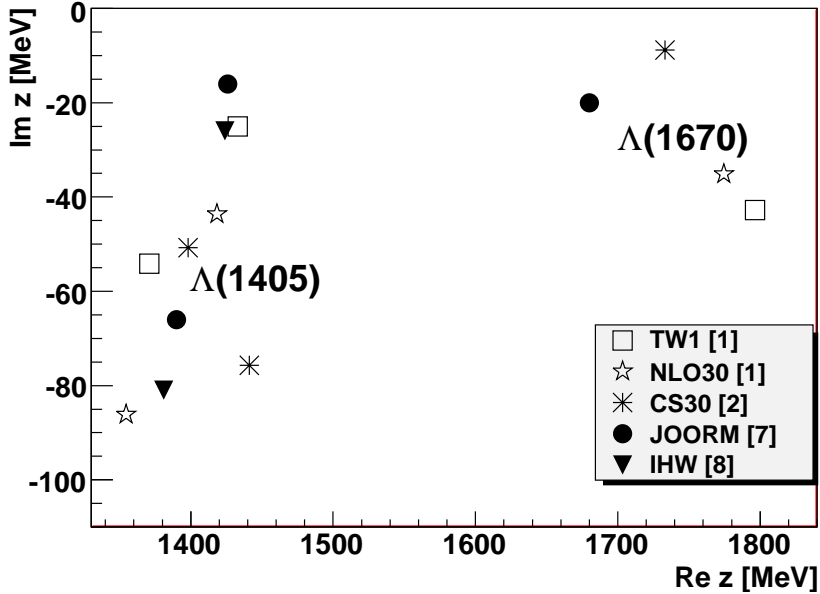
Figure 5.3: The positions of the isoscalar poles assigned to the $\Lambda(1405)$ and $\Lambda(1670)$ resonances in the TW1, NLO30 and CS30 models are shown in comparison with two other theoretical models JOORM [7] and IHW [8], [9]. Each model generates two poles assigned to the $\Lambda(1405)$ resonance.

the physical observables. The TW1 model generates the z_1 pole closest to the real axis of all discussed models at the position approximately $1371 - 54i$ MeV.

Surprisingly, the NLO corrections in the inter-channel couplings included in our NLO30 model shift both the z_1 and z_2 poles downwards to positions at energies $z_1 = 1355 - 86i$ MeV and $z_2 = 1418 - 44i$ MeV. This brings the z_2 pole in better agreement with the mass average 1405.1 ± 1.3 MeV reported in [11].

We do not show explicitly the results of the BNW model (Ref. [21]) in Figure 5.3 since there are results for more variants of the model depending on specific fit procedures. Instead, we try to summarize briefly their results and confront them with our predictions. Their Weinberg–Tomozawa model creates the poles at positions at $z_1 \approx 1391 - 55i$ MeV and $z_2 \approx 1431 - 17i$ MeV which agree with our TW1 model pretty well. It can be stated that the position of their z_1 pole is strongly model dependent and shifts far from the real axis once the NLO corrections are implemented. By contrast, the z_2 pole is more stable and its position do vary in some reasonable range. To sum it up, we are in nice agreement with the BNW model regarding the LO order of calculations. The changes of pole positions when including the NLO corrections show similar manner as in our case, though the shift

of the z_2 pole away from the real axis is not so large in the BNW model.

The $\Lambda(1405)$ spectrum produced by the NLO30 model is shown in the Figure 5.4 in comparison with mass distributions measured by various experiments [3], [4] and [5]. Theoretical prediction of the NLO30 model is pictured by solid curve which is obtained by setting the relative couplings $r_{\bar{K}N}/\pi\Sigma$ of the $\bar{K}N$ and $\pi\Sigma$ channels to get a peak at 1395 MeV. The two dashed lines introduce borders on the position of the peak (the other low energy constants stay fixed) since they represent the situation when the $\Lambda(1405)$ couples exclusively either to the $\pi\Sigma$ channel or to the $\bar{K}N$ channel.
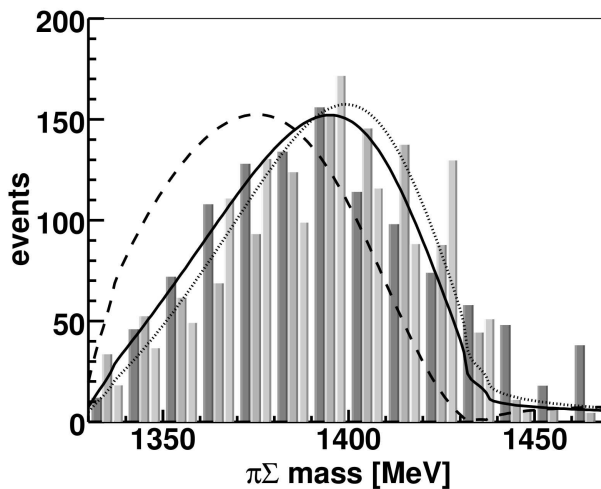
Figure 5.4: The $\pi\Sigma$ mass distribution. Results of NLO30 model are compared with the experimental data taken from Refs. [3], [4] and [5] with the experimental bars at each energy shown in this order. See the text for explanation on the theoretical curves obtained with the NLO30 model [10].

5.2.2 $\Lambda(1670)$

The isoscalar z_3 pole was found on the $[---+]$ Riemann sheet for the LO model TW1 and on the $[----]$ Riemann sheet in NLO models CS30 and NLO30. As we see in Figure 5.3, the z_3 pole was is located at rather varied positions for all considered models. We identify it with the $\Lambda(1670)$ resonance. All our models (TW1, NLO30 and CS30) generate the pole at energies about 50-100 MeV higher than the PDG value of the $\Lambda(1670)$ mass. The TW1 model gives the z_3 pole at position $1797 - 43i$ MeV and NLO corrections shift the pole slightly to lower energies at the position $1774 - 35i$ MeV in case of the NLO30 model and to the position at $1733 - 9i$ MeV for the CS30 model. Nevertheless, we would like

to emphasize that our models are fitted to the $\bar{K}N$ threshold data, and thus we do not expect the models to work so well at higher energies.

The resonant pole related to the $\Lambda(1670)$ resonance was predicted by the JOORM model too. Evidently, we observe the same pole as they do. Though their model produces the pole at a position that agrees much better with the experimental mass of the the $\Lambda(1670)$ resonance.

5.2.3 Isovector states

In this part we briefly discuss the generated isovector poles and their relation to physical observables. The assignment of the isovector poles to experimentally measured resonances presented in Table 5.2 is mostly tentative due to poor experimental data in this sector and we leave the interpretation of the $I = 1$ poles more or less open to further discussion.

Looking at the Table 5.2, we find three isovector poles z_4, z_5, z_6 on the Riemann sheets $[- - + + +]$, $[+ + - + +]$ and $[+ + + + -]$, respectively. For now, we leave out the z_4 and z_5 poles from our discussion, since they are located too far from the physical sheet to have any relevance for physical reality. Only the z_6 pole lies in such position on the complex energy manifold that it could be eventually a source of some resonance. Although the pole is located on a distant unphysical sheet, its position close to the $K\Xi$ threshold makes the trajectory path to the physical sheet not so long. According to the Re z_6, the possible candidate for dynamically generated resonance could be the $\Sigma(1750)$ state. In addition, the experimentally measured width is spanned from 60 MeV to 160 MeV which conforms well to the distance of the z_6 pole from the physical sheet. Coincidentally, the $\Sigma(1750)$ resonance is experimentally well established and because our predictions sufficiently agree on mass and width of the $\Sigma(1750)$ resonance, we dare to relate the z_6 pole with this resonance.

It is difficult to relate the z_5 and z_6 poles to any observed resonance. The pole z_5 leads to a "cusp structure" in energy dependence of the K^-n amplitude, see [23].

5.3 Movement of poles on Riemann sheets

As the parameters of the model are varied the pole moves in the complex energy plane. While a resonant pole moves on the negative half of the energy plane, its conjugate pole moves symmetrically above the real axis. Upon the movement, the poles can even get from the Riemann sheet to another by crossing the real axis through some of the branch

cuts associated with energy thresholds. In this case, the original resonant pole continues its movement on upper half energy plane of the new Riemann sheet and the original conjugate pole moves symmetrically on the lower half plane.

There is a rule that defines how Riemann sheets are linked together. A pole crossing the real axis above the k-th threshold ($k \leq N$) moves onto the Riemann sheet labeled by the first k signs opposite to those previous Riemann sheet and the remaining signs (for $i > k$). If pole crosses the cut twice it is the same as not crossing it. The simplified version of pole movement considering three channel thresholds is visualized in the Figure 5.5.
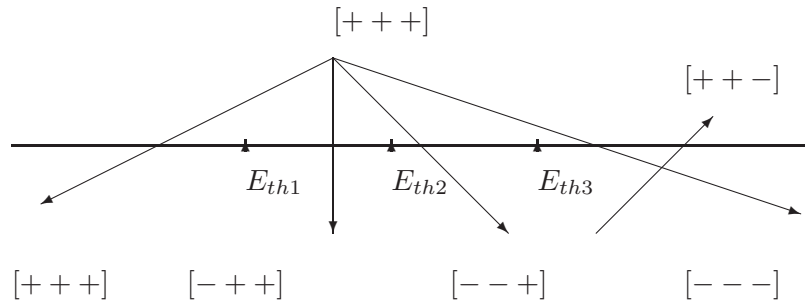
Figure 5.5: An example of pole movements from one Riemann sheet to another one for a three channel case. The symbol E_{th} denotes threshold of a specific channel associated with the pertinent branch cut.

A special situation occurs when a pole and its conjugate pole meet under all energy thresholds. Then both poles remain on the original Riemann sheet one of them moving along the real axis towards larger energies while the other pole moves towards lower energies. The poles move in this way until encounter any other singularity. Then there are two possibilities, what can happen. If any of the poles meet some another pole on the real axis, then they create a conjugate pair. One of the poles moves up to the upper half plane and the other moves down to the lower half plane. The second possibility is that the pole while moving along the real axis up meets the first energy threshold and than it is reflected back to move on the real axis in the opposite direction (on the Riemann sheet with the first sign opposite). At any case the only way to change the Riemann sheet is the crossing of the real axis a channel threshold or by catching a threshold while moving up along the real axis.

5.3.1 Zero coupling limit

In this section we investigate what happens with poles if the nondiagonal terms of potential matrix are switched off. In other words, the zero coupling limit means that we do not consider any coupling to different decay channels and keep only diagonal couplings in potential matrix intact. This approach was used for the first time in Ref. [71]. Afterwards it was applied on $\bar{K}N$ interaction to identify the origin of the z_1 and z_2 poles related to the $\Lambda(1405)$ resonance in models with energy dependent potential matrix [72]. In order to connect correctly the physical position of the poles with those in the zero coupling limit, we gradually reduce the scaling factor x which multiplies the interchannel couplings $x \cdot C_{ij}$ for $i \neq j$ where $0 \leq x \leq 1$ and follow the pole trajectories in the complex energy plane. The scaling parameter x has a value 1 for physical coupling and value 0 in the zero coupling limit, in which only the diagonal Clebsh–Gordan coefficients (C_{ij} for $i = j$) may stay nonzero.

The positions of poles in the zero coupling limit is determined by a condition

$$\prod_n [1/v_{nn} - G_n] = 0, \tag{5.2}$$

where G_n stands for a Green function (4.8). Substituting the separable potential in the previous equation we get

$$\frac{4\pi f_\pi^2}{C_{nn}} \frac{z}{M_n} + G_n(z) = 0. \tag{5.3}$$

Since the isospin symmetry is broken for $x < 1$ in the physical base of channels and thus it is not possible to define a proper isospin there, the further analysis of pole movements is performed either in the isoskalar or in the isovector base. Moreover, the pole trajectories on the complex energy manifold are much easier to follow if one considers only four or five energy thresholds, respectively.

To manifest results of our analysis we chose the recent NLO30 model as a representative example. In Figure 2 we visualize trajectories of the isoscalar and isovector poles as we gradually reduce the parameter x from its physical value to the zero coupling limit. In the left panel, the trajectories of isovector poles assigned to $\Lambda(1405)$ and $\Lambda(1670)$ resonances are shown. As we already know, the $\Lambda(1405)$ is represented by two poles, z_1 and z_2. For physical couplings we found both poles on the $[-+++]$ Riemann sheet when searching for them in the amplitudes of the $\pi\Sigma$ and $\bar{K}N$ channels since the z_1 and z_2 poles have considerable couplings to these channels. The results of the TW1 model and the CS30
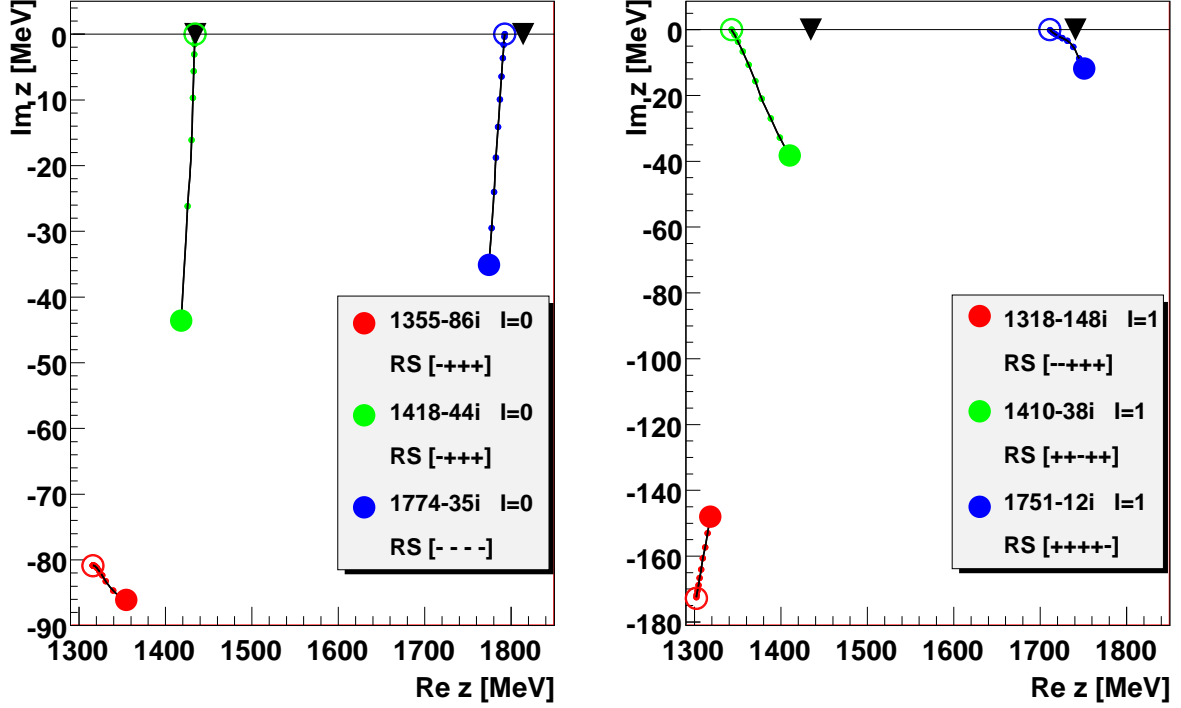
Figure 5.6: Pole movements upon scaling the nondiagonal interchannel couplings in the NLO30 model. Left panel: isoscalar states ($I = 0$), right panel: isovector states ($I = 1$). The large solid and empty circles show the pole positions in the physical and zero coupling limits, respectively. The black triangles mark the $\bar{K}N$ and $K\Xi$ thresholds in the isoscalar case and the $\bar{K}N$ and $\eta\Sigma$ thresholds in the isovector case. Energies of the thresholds are $E_{\bar{K}N} = 1434.6$ MeV, $E_{\eta\Sigma} = 1740.6$ MeV and $E_{K\Xi} = 1814.0$ MeV. The Riemann sheets the poles move on are specified in the legend.

model are given in Appendix.

As we gradually reduce the scaling factor x, the z_1 pole vanishes in the $\bar{K}N$ amplitude and and conversely the z_2 disappears in the $\pi\Sigma$ amplitude. In this way, we are able to assign the pole to pertinent channel. The z_1 pole terminates its movement at a position with a large imaginary part of the complex energy in the $\pi\Sigma$ channel and thus it is interpreted as resonance in the zero coupling limit. On the other hand, by reducing the nondiagonal potential terms the z_2 pole develops to the real axis and finishes its movement for $x = 0$ slightly under the $\bar{K}N$ threshold, at energy $E_{\bar{K}N} \approx 1434.59$ MeV. Thus the z_2 pole is referred to be $\bar{K}N$ bound state in the zero coupling limit. Since the pole stays on the $[- + ++]$ Riemann sheet, which is unphysical in the $\pi\Sigma$ channel, but physical in the $\bar{K}N$

channel, its final position in the zero coupling limit can be identified with a $\bar{K}N$ bound state. This conclusion is in agreement with other theoretical studies.

A similar picture of the trajectory path was observed in all our models, although the final position in the zero coupling limit is sometimes very tightly below the $\bar{K}N$ threshold. See the Table 5.3 for more details.

The situation for the z_3 pole assigned to the $\Lambda(1670)$ resonance varies with the used models. In the TW1 model, the z_3 pole lies on the $[- - - +]$ Riemann sheet and for $x = 0$ it terminates on the real axis at energy $E \approx 1792.6$ MeV below the $K\Xi$ threshold. The pole is determined to be $K\Xi$ bound state since the Riemann sheet $[- - - +]$ is physical in the $K\Xi$ channel. A different situation is observed in the NLO models NLO30 and CS30. There, the z_3 pole ends its movement under the $K\Xi$ threshold too, but on the $[- - - -]$ Riemann sheet, which is unphysical in the $K\Xi$ channel. Thus the pole terminates as $K\Xi$ quasi-bound state in the NLO30 and CS30 model.

The trajectory path of our three $I = 1$ poles is shown in the right panel of the Figure 2. In the zero coupling limit, the poles z_4, z_5 and z_6 couple to channels $\pi\Sigma$, $\bar{K}N$ and $K\Xi$, respectively. The situation for the z_4 pole, which is observed in the $[- - + + +]$ Riemann sheet, is very similar to the one observed for the isoscalar z_1 pole. When the parameter x is reduced, the z_4 pole moves away from the real axis to the point $1301.9 - 172.8i$ MeV and thus it is a resonance in the zero coupling limit. In the zero coupling limit, the z_5 pole gets on the real axis under the $\bar{K}N$ threshold on the Riemann sheet $[+ + - + +]$. The third pole z_6 develops under the $\eta\Sigma$ threshold on the unphysical Riemann sheet.

Figure 5.7 demonstrates the sensitivity of our results to the considered models. The poles related to the $\Lambda(1405)$ resonance were chosen for the comparison. We see that the final position of the z_2 pole is not model dependent and the pole terminates always slightly under the $\bar{K}N$ threshold although its trajectory does vary to some extend for $x > 0$. On the other hand, the position of the z_1 pole in the zero coupling limit varies significantly on the model.

5.3.2 SU(3) symmetry breaking

Inspired by the Ref. [7], we investigate pole origins in the limit of the $SU(3)$ symmetry restoration. This limit is simulated by setting all the masses of the mesons and of the baryons to their respective values assumed for the $SU(3)$ symmetry limit. We adopted the same values as those established in Ref. [7], $m_0 = 370$ MeV for mesons and $M_0 = 1115$ MeV for baryons. Since the effective chiral Lagrangian represents an interaction of meson octet
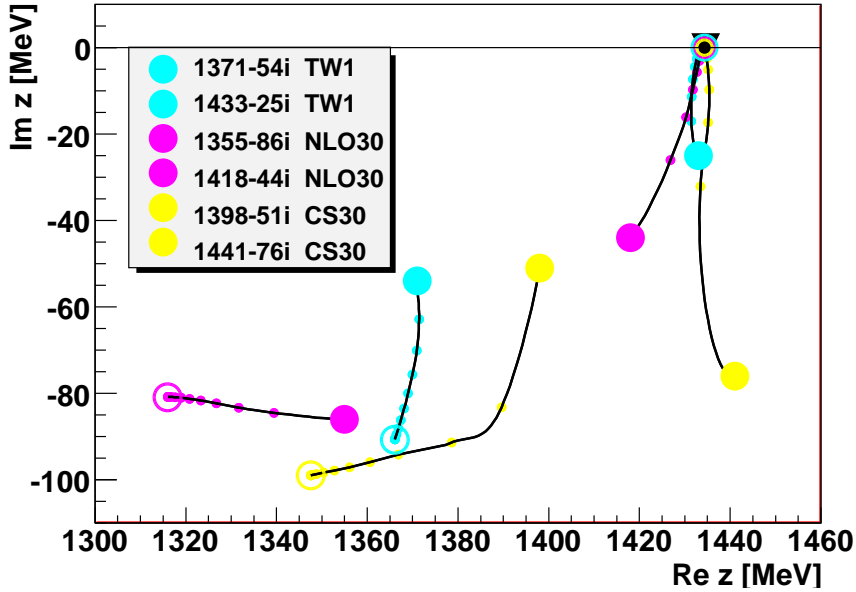
Figure 5.7: The trajectories of the $I = 0$ poles related to the $\Lambda(1405)$ resonance upon scaling the nondiagonal interchannel couplings for the TW1, NLO30 and CS30 models. The large solid and empty circles show the pole positions in the physical and zero coupling limits, respectively. The black triangles mark the $\bar{K}N$ threshold. The poles move on the $[-+++]$ Riemann sheet.

with baryon octet, the $SU(3)$ decomposition into irreducible representations reads

$$8 \otimes 8 = 1 \oplus 8_s \oplus 8_a \oplus 10 \oplus \overline{10} \oplus 27, \tag{5.4}$$

where only interactions in the singlet and two octets are attractive, so we do not expect any bound states in the 10, $\overline{10}$ and 27 representations. On top of that the symetric and antisymmetric octets are assumed to be degenerate. Therefore in the limit of $SU(3)$ symmetry restoration, only two poles related to the to singlet and octet state should be found.

The pole movements are followed as the $SU(3)$ symmetry is gradually restored by scaling the physical masses using the following relations

$$
\begin{aligned}
M_i(x) &= M_0 + x_{SU3}(M_i - M_0) \\
m_i^2(x) &= m_0^2 + x_{SU3}(m_i^2 - m_0^2),
\end{aligned}
\tag{5.5}
$$
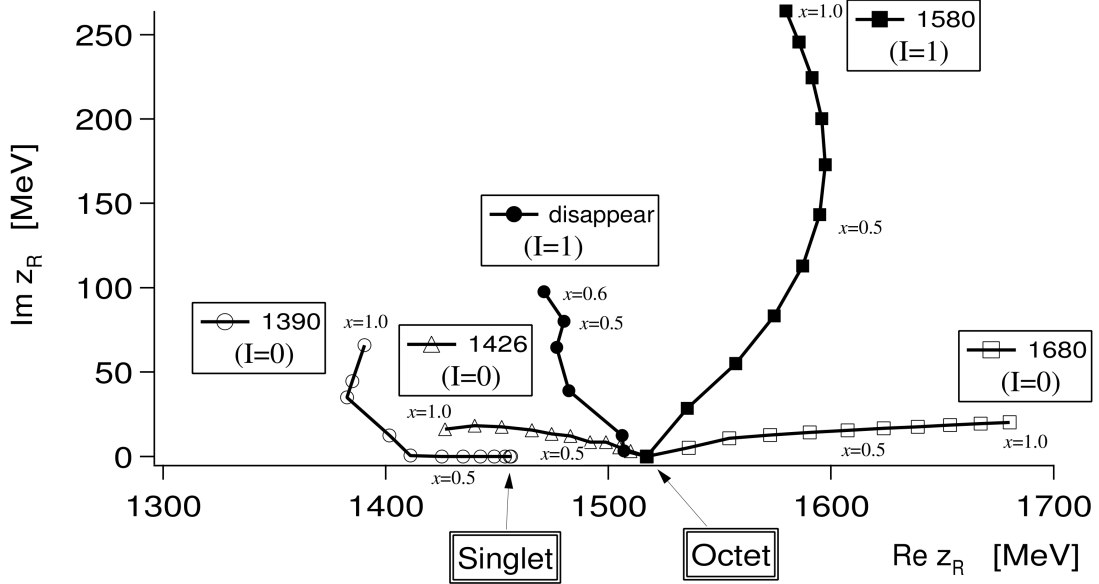
Figure 5.8: Trajectories of the poles in the scattering amplitudes obtained by varying gradually the $SU(3)$ breaking parameter x_{SU3}. At the $SU(3)$ symmetric limit ($x_{SU3} = 0$), only two poles appear, one is for the singlet and another one for the octet. The symbols correspond to the step size $\delta x = 0.1$.[7]

where M_i and m_i denote the physical baryon and meson masses. We vary the scaling factor x_{SU3} from value $x_{SU3} = 1$, which represents the physical limit of a broken $SU(3)$ symmetry to $x_{SU3} = 0$ standing for $SU(3)$ limit. It is important to stress that not only poles but also the energy thresholds of considered channels move as we scale the masses from their physical values into the $SU(3)$ limit and finally there is only one threshold at 1520 MeV.

Let's firstly have a look at results of JOORM model visualized in Figure 5.8, where trajectories of the $I = 0$ and $I = 1$ poles evolve from the $SU(3)$ limit to their physical positions. We should remark that, in picture 5.8, poles from various Riemann sheets are visualized together and moreover the trajectories of conjugate poles are depicted instead of resonant poles. However, this makes no difference since the movement of resonant an its conjugate poles is symmetric. They evidently observed that the pole of the $\Lambda(1405)$ resonance in lower energies comes from the point on the real axis around 1450 MeV($x_{SU3} <$ 0.6) which is assigned to the singlet state. The common origin of poles around 1510 MeV is assigned to the octet state and by going to the physical masses this pole splits apart in four
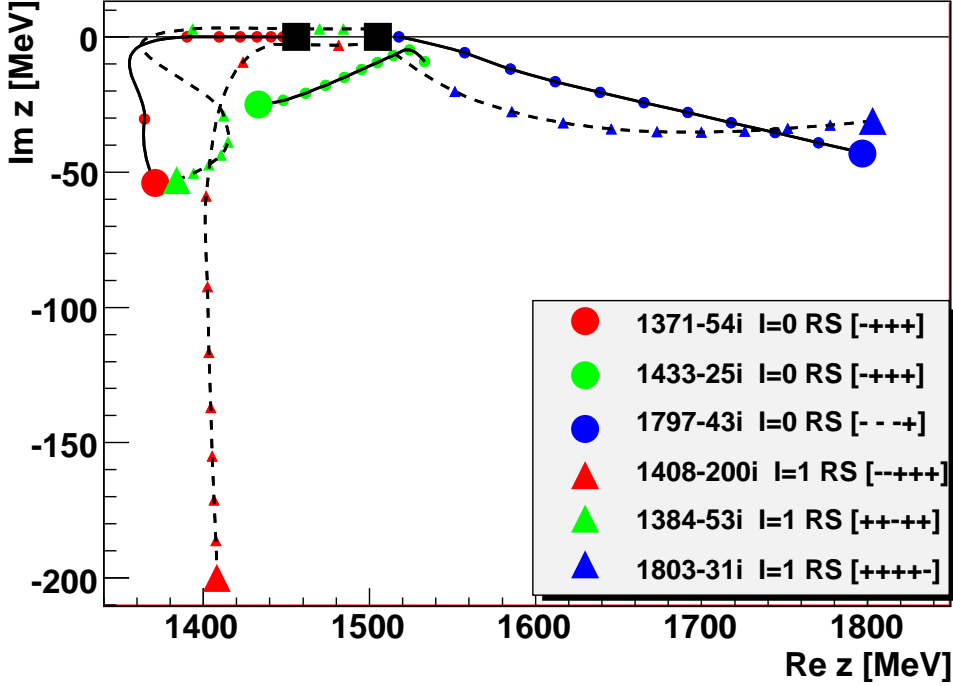
Figure 5.9: Trajectories of isoscalar (continuous lines) and isovector (dashed lines) poles obtained by varying the $SU(3)$ scaling parameter from $x_{SU3} = 1$ to $x_{SU3} = 0$. Full circles ($I = 0$) and triangles ($I = 1$) correspond to physical values of meson and baryon masses, the full squares represent the positions of the $SU(3)$ singlet and octet states in the $SU(3)$ restoration limit.

branches. In physical limit, the two isoscalar states are related with the $\Lambda(1670)$ resonance and the higher pole of the $\Lambda(1405)$. Then two isoscalar poles are observed but one of these poles were not followed up to its physical limit since it disappeared for $x_{SU3} \approx 0.6$.

Looking at the Figure 5.9, we find that compared to the work [7], we observe one additional $I = 1$ pole and none of our isovector poles get lost on its way to the physical limit. On the contrary, the scenario of trajectory path of isoscalar poles is similar to the one in reported in Ref. [7].

At this point, we try to explain the disappearance of the $I = 1$ pole in Figure 5.9 by making our own analysis with our TW1 model and comparing our results with those of authors of Ref. [7]. The TW1 model provides the most appropriate comparison since it is also based on the leading Weinberg-Tomozawa term of the chiral Lagrangian. The pole trajectories to the $SU(3)$ symmetric limit in our model are showed in Figure 5.9. We successfully reproduce the singlet and octet states in the $SU(3)$ symmetry restoration with
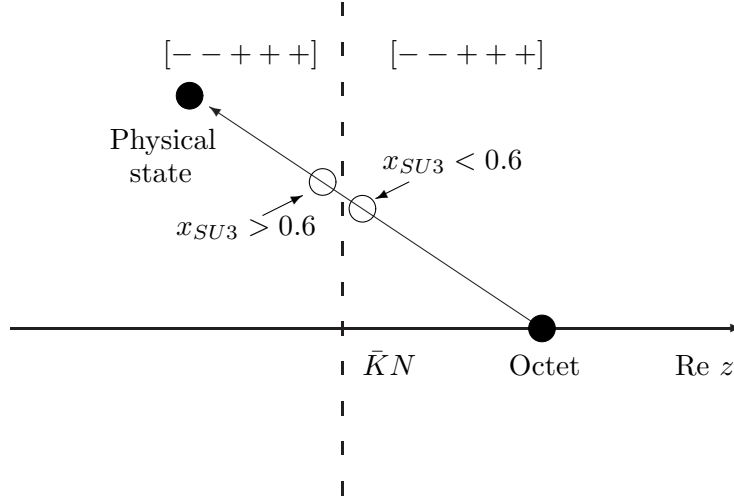
Figure 5.10: Drawing a of situation related to the disappearence of the pole for $x_{SU3} \approx 0.6$ in Figure 5.9. The pole trajectory from the $SU(3)$ symmetric limit (full circle on real axis) to the physical state (full circle). The dashed line denotes the $\bar{K}N$ threshold. The open circles denote positions of poles for the value of x_{SU3} slightly smaller than 0.6 ($x_{SU3} < 0.6$) and for x_{SU3} slightly larger than 0.6 ($x_{SU3} > 0.6$). and simultaneously the border of Riemann sheets, how it was defined by authors [7]. The symbol $[- - + + +]$ denotes the Riemann sheet on which the pole moves in reality.

our TW1 model. The singlet pole is observed at 1455 MeV and and the octet pole at a position approximately 1505 MeV. The fact that the poles do not finish exactly at the same point may come from the phase transition which emerges in the moment of the $SU(3)$ symmetry restoration. To be more precise, the phase transition occurs when we change the value of x_{SU3} from a very small number to zero, and thus the number of channels suddenly changes from N channels to 1 channel.

The trajectories of isoscalar poles are quite analogous to those in Ref. [7], although the exact pole positions are different to some extend. Let's have a look at the $I = 1$ poles. We believe that the disappearance of one isovector pole in Figure 5.9, can be attributed to the method they treated the Riemann sheets. We offer possible explanation of this issue in Figure 5.10 where the pole trajectory with the labeled Riemann sheets is pictured in a detail.

Looking at the Figure 5.10, we see that the pole develops from its origin in the octet state and moves away from the real axis on the Riemann sheet $[- - + + +]$. Considering the fact that the pole disappeared for $x_{SU3} \approx 0.6$ where the real part of the complex energy

is equal to shifted threshold energy in the KN channel we dare to say that the authors of Ref. [7] lost the pole due to switching on a wrong Riemann sheet at the threshold energy. They probably switch on the Riemann sheet $[-++++]$ at the energy of the $\bar{K}N$ threshold (the border is marked by the dashed line in the Figure 5.10). The problem is that the only way to change the Riemann sheet is by crossing over the appropriate branch cut associated with threshold energies on the real axis. It is evident that the trajectory path do not cross any branch cuts on its way to physical state, and thus there is no reason to change the Riemann sheet at the moment. The whole trajectory of the pole should be observed on same Riemann sheet $[--+++]$.

PDG			Model					
			TW1		**NLO30**		**CS30**	
Resonance	Γ[MeV]	Decay channels	Position	RS	Position	RS	Position	RS
$\Lambda(1405)$ ****	50	$\pi\Sigma$	$1371 - 54i$	$[-+++]$	$1355 - 86i$	$[-+++]$	$1398 - 51i$	$[-+++]$
			$1433 - 25i$	$[-+++]$	$1418 - 44i$	$[-+++]$	$1441 - 76i$	$[-+++]$
$\Lambda(1670)$ ****	35	$\pi\Sigma,\bar{K}N,\eta\lambda$	$1797 - 43i$	$[---+]$	$1774 - 35i$	$[----]$	$1733 - 9i$	$[----]$
$\Lambda(1800)$ ***	300	$\pi\Sigma,\bar{K}N$						

Table 5.1: Comparison of s-wave resonances with the $S = -1$ strangeness and the $I = 0$ isospin measured by experiment [11] and predictions on pole positions of our TW1, NLO30 and CS30 models. The real part of complex energy corresponds to the energy of the resonance, the imaginary part of the energy is approximately a half of resonant width. RS denotes the Riemann sheet - specified by the signs in the squared brackets.

PDG			Model					
			TW1		**NLO30**		**CS30**	
Resonance	Γ[MeV]	Decay channels	Position	RS	Position	RS	Position	RS
$\Lambda(1480)$ *	55	$\bar{K}N,\pi\Sigma,\pi\Lambda$	$1408 - 200i$	$[--+++]$	$1318 - 148i$	$[--+++]$	$1336 - 220i$	$[--+++]$
$\Lambda(1560)$ **	79	$\pi\Sigma,\ \pi\Lambda$	$1384 - 53i$	$[++-++]$	$1410 - 38i$	$[++-++]$	$1416 - 24i$	$[++-++]$
$\Sigma(1620)$ **	60	$\bar{K}N,\pi\Sigma,\ \pi\Lambda$						
$\Sigma(1750)$ ***	90	$\bar{K}N,\pi\Sigma,\pi\Lambda$	$1803 - 31i$	$[++++-]$	$1751 - 12i$	$[++++-]$	$1799 - 2i$	$[++++-]$

Table 5.2: Comparison of s-wave resonances with the $S = -1$ strangeness and the $I = 1$ isospin measured by experiment [11] and predictions on pole positions of our TW1, NLO30 and CS30 models. The real part of complex energy corresponds to the energy of the resonance, the imaginary part of the energy is approximately a half of the resonant width. RS denotes the Riemann sheet - specified by the signs in the squared brackets.

Pole	TW1			NLO30			CS30		
	Position	RS	Channel	Position	RS	Channel	Position	RS	Channel
z_1	$1366.1-90.7i$	$[-+++]$	$\pi\Sigma$	$1316.1-80.9$	$[-+++]$	$\pi\Sigma$	$1347.6-99.0i$	$[-+++]$	$\pi\Sigma$
z_2	$1433.8-0.0i$	$[-+++]$	$\bar{K}N$	$1434.3-0.0i$	$[-+++]$	$\bar{K}N$	$1434.58-0.0i$	$[-+++]$	$\bar{K}N$
z_3	$1809.0-0.0i$	$[---+]$	$K\Xi$	$1792.6-0.0i$	$[----]$	$K\Xi$	$1734.4-0.0i$	$[----]$	$K\Xi$

Table 5.3: Final positions of the $I=0$ poles and their assignment to pertinent channels in the zero coupling limit are compared for the TW1, NLO30 and CS30 models, RS denotes the Riemann sheet - specified by the signs in the squared brackets. The energies of the thresholds are $E_{\bar{K}N} = 1434.59$ MeV and $E_{K\Xi} = 1814.0$ MeV.

Pole	TW1			NLO30			CS30		
	Position	RS	Channel	Position	RS	Channel	Position	RS	Channel
z_4	$1386.8-219.9i$	$[--+++]$	$\pi\Sigma$	$1301.9-172.8i$	$[--+++]$	$\pi\Sigma$	$1311.2-224.8i$	$[--+++]$	$\pi\Sigma$
z_5	$1157.7-17.9i$	$[++-++]$	$\bar{K}N$	$1342.8-0.0i$	$[++-++]$	$\bar{K}N$	$1376.0-0.0i$	$[++-++]$	$\bar{K}N$
z_6	$1657.7-0.0i$	$[++++-]$	$\eta\Lambda$	$1711.0-0.0i$	$[++++-]$	$K\Xi$	$1760.5-0.0i$	$[++++-]$	$K\Xi$

Table 5.4: Final positions of the $I=1$ poles and their assignment to pertinent channels in the zero coupling limit are compared for the TW1, NLO30 and CS30 models, RS denotes the Riemann sheet - specified by the signs in the squared brackets. The energies of the thresholds are $E_{\bar{K}N} = 1434.59$ MeV, $E_{\eta\Sigma} = 1740.6$ MeV.

Chapter 6

Conclusion

In this thesis, we studied dynamically generated meson–baryon resonances in framework of chirally motivated a coupled channel approach. Our technique for analysis of the scattering amplitude is based on modern collision theory which describes the resonant states as poles on specific unphysical Riemann sheets of the complex energy manifold. We presented predictions for s-wave resonances with the $S = -1$ strangeness and the $I = 0$, 1 isospins in range of energies 1300-1800 MeV. We also discussed the current status of the experimental and theoretical understanding of relevant resonances including not only other chiral approaches but also alternative baryon models. Hereby, we presented a detailed view on this topic.

Results of chiral model based on the leading order Weinberg–Tomozawa interaction and on two models that include terms up to second order of effective chiral Lagrangian in external meson momenta were discussed in comparison with experimentally measured resonances listed in Particle Data Group (PDG) as well as predicted by other chirally motivated models. We achieved a satisfactory results already with the LO chiral model and incorporated NLO corrections were in agreement with previous results.

Summing our results up were achieved the following:

- Excellent predictions were obtained for the $\Lambda(1405)$ resonance observed in the $\pi\Sigma$ mass spectrum by all used models. We confirmed that there are two poles in the complex energy plane whose positions can be related to the properties of the $\Lambda(1405)$ resonance established by the PDG. As an example for all models, the poles were generated by the NLO30 model at positions $z_1 \approx 1355 - 86i$ MeV and $z_2 \approx 1418 - 44i$ MeV. A good reproduction of the $\pi\Sigma$ mass spectrum was achieved.

- Less convincing results were achieved for the $\Lambda(1670)$ resonance which was found about 50-100 MeV higher (depending on used model) than the experimentally established mass of the resonance. For instance, the NLO30 model creates the pole at position $z_3 \approx 1774 - 35i$ MeV. This can be attributed to the fact that models are fitted to the low energy $\bar{K}N$ threshold data, and consequently the models do not have such predictive power at higher energies.

- Similarly, we found three isovector poles in the examined range of energies 1300 - 1800 MeV, but two of them are very far from the physical region that they can hardly affect any physical observables. Only one isovector pole with its position at $z_6 \approx 1751 - 12i$ MeV on the further Riemann sheet can be assigned, by all appearance, to the $I = 1$ resonance $\Sigma(1750)$.

By examining the pole movements on the complex energy manifold into the zero coupling limit and into $SU(3)$ symmetry restoration limit, we obtained an additional valuable information about origin of the poles.

- In the zero coupling limit, we found that the $\Lambda(1405)$ pole lying at lower energies originates from the resonance in the $\pi\Sigma$ channel and the pole at higher energies develops from the $\bar{K}N$ bound state. The pole related to the resonances $\Lambda(1670)$ can trace its origin either to the $K\Xi$ bound state or to the $K\Xi$ quasi-bound state depending on a model.

- In the limit of $SU(3)$ symmetry restoration, a common origin of poles related to the singlet and octet states were confirmed. The singlet pole develops to the lower pole of the $\Lambda(1405)$ resonance and octet state is origin of all other observed poles.

To conclude, we would like to underline that chiral models provide a new perspective on the problematic of strange $S = -1$ baryon resonances in the low energy spectra and they considerably contribute to understanding of their nature. This approach was especially successful by examining the $\Lambda(1405)$ resonance, whose two pole structure is now widely supported by several chirally motivated models.

Bibliography

[1] M. Niiyama et al. Photoproduction of Lambda(1405) and Sigma(1385) on the proton at E = 1.5-2.4 GeV. *Phys. Rev.*, 2008.

[2] J. K. Ahn. Lambda(1405) photoproduction at SPring-8/LEPS. *Nucl. Phys.*, A721: 715–718, 2003.

[3] D. W. Thomas, A. Engler, H. E. Fisk, and R. W. Kraemer. Strange particle production from $\pi^- p$ interactions at 1.69 gev/c. *Nucl. Phys.*, B56:15–45, 1973.

[4] R. J. Hemingway. Production of Lambda(1405) in $K^- p$ reactions at 4.2- GeV/c. *Nucl. Phys.*, B253:742, 1985.

[5] I. Zychor et al. Shape of the Lambda(1405) hyperon measured through its $\Sigma^0 \pi^0$ decay. *Phys. Lett.*, B660:167–171, 2008.

[6] A. Cieply and J. Smejkal. Separable potential model for $K^- N$ interactions at low energies. *Eur. Phys. J.*, A43:191–208, 2010.

[7] D. Jido, J. A. Oller, E. Oset, A. Ramos, and U. G. Meissner. Chiral dynamics of the two Lambda(1405) states. *Nucl. Phys.*, A725:181–200, 2003.

[8] Yoichi Ikeda, Tetsuo Hyodo, and Wolfram Weise. Improved constraints on chiral SU(3) dynamics from kaonic hydrogen. *Phys.Lett.*, B706:63–67, 2011.

[9] Yoichi Ikeda, Tetsuo Hyodo, and Wolfram Weise. Chiral su(3) theory of antikaon-nucleon interactions with improved threshold constraints. *Prerint submitted to Nucl.Phys.*, A, 2011.

[10] A. Cieply and J. Smejkal. Chirally motivated $\bar{K}N$ amplitudes for in-medium applications. *Nucl. Phys.*, A 188:115–126, 2012.

[11] K. Nakamura et al. Review of particle physics. *J. Phys.*, G37:075021, 2010. URL `http://pdg.lbl.gov/`.

[12] A. V. Anisovich, V. V. Anisovich, M. A. Matveev, V. A. Nikonov, J. Nyiri, and A. V. Sarantsev. *MESONS and BARYONS Systematization nad Methods of Analysis*. World Scientific Publishing, 2008.

[13] Steven Weinberg. Phenomenological Lagrangians. *Physica*, A96:327, 1979.

[14] Jose A. Oller. On the strangeness -1 S-wave meson baryon scattering. *Eur. Phys. J.*, A28:63–82, 2006.

[15] Waas T., Kaiser N., and Weise W. Low energy $\bar{K}$n interaction in nuclear matter. *Phys. Let. B, 365*, 1995.

[16] N. Suzuki, T. Sato, and T. S. H. Lee. Extraction of Resonances from Meson-Nucleon Reactions. *Phys. Rev.*, C79:025205, 2009.

[17] E. Oset et al. Dynamically generated resonances in the chiral unitary approach to meson baryon interaction. *Int. J. Mod. Phys.*, A20:1619–1626, 2005.

[18] E. Oset, V. K. Magas, and A. Ramos. On the nature of the Lambda(1405) as a superposition of two states. *AIP Conf. Proc.*, 842:455–457, 2006.

[19] R. Nißler. *Topics in three flavor chiral dynamics*. PhD thesis, Rheinischen Friedrich-Wilhelms-Universit¨at Bonn, 2008. URL `http://hss.ulb.uni-bonn.de/2008/1316/1316.htm`.

[20] C. Garcia-Recio, J. Nieves, E. Ruiz Arriola, and M. J. Vicente Vacas. $S = -1$ Meson-Baryon Unitarized Coupled Channel Chiral Perturbation Theory and the $S_{01}-\Lambda(1405)$ and $-\Lambda(1670)$ Resonances. *Phys. Rev.*, D67:076009, 2003.

[21] B. Borasoy, R. Nissler, and W. Weise. Chiral dynamics of kaon nucleon interactions, revisited. *Eur. Phys. J.*, A25:79–96, 2005.

[22] Norbert Kaiser, P. B. Siegel, and W. Weise. Chiral dynamics and the low-energy kaon - nucleon interaction. *Nucl. Phys.*, A 594:325–345, 1995.

[23] A. Cieply and J. Smejkal. Chiral model for $\bar{K}N$ interactions and its pole content. *AIP Conf. Proc.*, 1322:364–368, 2010.

[24] Margaret H. Alston et al. Study of Resonances of the $\Sigma^-\pi$ System. *Phys. Rev. Lett.*, 6:698–702, 1961.

[25] C. Caso et al. Review of particle physics. *Eur. Phys. J.*, C3:1–794, 1998. URL `http://pdg.lbl.gov/`.

[26] R. H. Dalitz and A. Deloff. The Shape and parameters of the Lambda(1405) resonance. *J. Phys.*, G17:289–302, 1991.

[27] Tetsuo Hyodo and Daisuke Jido. The nature of the Lambda(1405) resonance in chiral dynamics. *Prog. Part. Nucl. Phys.*, 67:55–98, 2012.

[28] V. K. Magas, E. Oset, and A. Ramos. Evidence for the two pole structure of the Lambda(1405) resonance. *Phys. Rev. Lett.*, 95:052301, 2005.

[29] S. Prakhov et al. $K^-p \to \pi^0\pi^0\Sigma^0$ at $p(K^-)$ = 514-MeV/c to 750-MeV/c and comparison with other π^0 π^0 production. *Phys. Rev.*, C70:034605, 2004.

[30] T. Hyodo, A. Hosaka, E. Oset, A. Ramos, and M. J. Vicente Vacas. Lambda(1405) production in the $pi^-p \to k^0\pi\sigma$ reaction. *Phys. Rev.*, C68:065203, 2003.

[31] T. Hyodo, A. Hosaka, M. J. Vicente Vacas, and E. Oset. Photoproduction of k* for the study of lambda(1405). *Phys. Lett.*, B593:75–81, 2004.

[32] J. C. Nacher, E. Oset, H. Toki, and A. Ramos. Photoproduction of the lambda(1405) on the proton and nuclei. *Phys. Lett.*, B455:55–61, 1999.

[33] G. P. Gopal et al. Partial Wave Analyses of $\bar{K}N$ Two-Body Reactions Between 1480-MeV and 2170-MeV. *Nucl. Phys.*, B119:362, 1977.

[34] H. Koiso, F. Sai, S. S. Yamamoto, and R. R. Kofler. Search for the P11 Sigma(1660) resonance in the reactions $K^-p \to \Sigma^\pm\pi^\mp$ in the momentum range 597-MeV/c to 888-MeV/c. *Nucl. Phys.*, A433:619, 1985.

[35] V. Hepp et al. New Data on the Reaction $K^-n \to (\Sigma\pi)^-$ and a Partial Wave Analysis of $\bar{K}N \to \Sigma\pi$ in the Energy Range 1520-MeV-1745-MeV. *Phys. Lett.*, B65:487, 1976.

[36] D. M. Manley et al. Properties of the Lambda(1670)(1/2)- resonance. *Phys. Rev. Lett.*, 88:012002, 2002.

[37] A. Starostin et al. Measurement of $K^-p \to \eta\Lambda$ near threshold. *Phys. Rev.*, C64: 055205, 2001.

[38] S. Prakhov et al. Measurement of K^-p radiative capture to $\gamma\Lambda$ and $\gamma\Sigma^0$ for p_{K^-} between 514 and 750 MeV/c. *Phys. Rev.*, C82:015201, 2010.

[39] M. D. Jones. A study of the reaction $K^-p \to \Sigma^0\eta$ near threshold. *Nucl. Phys.*, B73: 141–165, 1974.

[40] Simon Capstick and W. Roberts. Quark models of baryon masses and decays. *Prog. Part. Nucl. Phys.*, 45:S241–S331, 2000.

[41] Claude Amsler et al. Review of particle physics. *Phys. Lett.*, B667:1–1340, 2008. URL http://pdg.lbl.gov.

[42] Hael Collins and Howard Georgi. S_3 and the $L = 1$ baryons in the quark model and the chiral quark model. *Phys. Rev.*, D59:094010, 1999.

[43] Nathan Isgur and Gabriel Karl. Hyperfine Interactions in Negative Parity Baryons. *Phys. Lett.*, B72:109, 1977.

[44] Nathan Isgur and Gabriel Karl. P Wave Baryons in the Quark Model. *Phys. Rev.*, D18:4187, 1978.

[45] Simon Capstick and Nathan Isgur. Baryons in a Relativized Quark Model with Chromodynamics. *Phys. Rev.*, D34:2809, 1986.

[46] Derek B. Leinweber. QCD Sum Rule Analysis Of Spin-Orbit Splitting in Baryons. *Ann. Phys.*, 198:203, 1990.

[47] L. Ya. Glozman and D. O. Riska. The Spectrum of the nucleons and the strange hyperons and chiral dynamics. *Phys. Rept.*, 268:263–303, 1996.

[48] C. L. Schat, J. L. Goity, and N. N. Scoccola. Masses of the 70- baryons in large N(c) QCD. *Phys. Rev. Lett.*, 88:102002, 2002.

[49] N. Matagne and Fl. Stancu. SU(6) [**70**, 1^-] baryon multiplet in the $1/N_c$ expansion. *Phys. Rev.*, D83:056007, 2011.

[50] R. H. Dalitz, T. C. Wong, and G. Rajasekaran. Model calculation for Y*(0)(1405) resonance state. *Phys. Rev.*, 153:1617–1623, 1967.

[51] E. A. Veit, Byron K. Jennings, R. C. Barrett, and Anthony William Thomas. Kaon - Nucleon Scattering In An Extended Cloudy Bag Model. *Phys. Lett.*, B137:415, 1984.

[52] E. A. Veit, Byron K. Jennings, Anthony William Thomas, and R. C. Barrett. S Wave Meson - Nucleon Scattering In An SU(3) Cloudy Bag Model. *Phys. Rev.*, D31:1033, 1985.

[53] B. K. Jennings. Further Evidence On The Nature Of The Lambda(1405). *Phys. Lett.*, B176:229, 1986.

[54] K. Dannbom, E. M. Nyman, and D. O. Riska. Excited Hyperons In The Skyrme Model. *Phys. Lett.*, B227:291, 1989.

[55] Jr. Callan, Curtis G. and Igor R. Klebanov. Bound State Approach to Strangeness in the Skyrme Model. *Nucl. Phys.*, B262:365, 1985.

[56] A. Zhang et al. $J^{(P)} = (1/2)^-$ pentaquarks in Jaffe and Wilczek's diquark model. *High Energy Phys. Nucl. Phys.*, 29:250, 2005.

[57] Toru T. Takahashi and Makoto Oka. Low-lying Lambda Baryons with spin 1/2 in Two-flavor Lattice QCD. *Phys. Rev.*, D81:034505, 2010.

[58] Noriyoshi Ishii, Takumi Doi, Makoto Oka, and Hideo Suganuma. Five-quark picture of Lambda(1405) in anisotropic lattice QCD. *Prog. Theor. Phys. Suppl.*, 168:598–601, 2007.

[59] J. Gasser and H. Leutwyler. Chiral Perturbation Theory to One Loop. *Ann. Phys.*, 158:142, 1984.

[60] Elizabeth Ellen Jenkins and Aneesh V. Manohar. Baryon chiral perturbation theory using a heavy fermion Lagrangian. *Phys. Lett.*, B255:558–562, 1991.

[61] Stefan Scherer. Introduction to chiral perturbation theory. *Adv. Nucl. Phys.*, 27:277, 2003.

[62] A. Hosaka and H. Toki. *QUARKS, BARYONS AND CHIRAL SMMETRY*. World Scientific Publishing, 2001.

[63] Yoichi Ikeda, Tetsuo Hyodo, and Wolfram Weise. Improved constraints on chiral SU(3) dynamics from kaonic hydrogen. *Phys. Lett.*, B706:63–67, 2011.

[64] G. Beer et al. Measurement of the kaonic hydrogen X-ray spectrum. *Phys. Rev. Lett.*, 94:212302, 2005.

[65] M. Bazzi et al. A New Measurement of Kaonic Hydrogen X rays. *Phys. Lett.*, B704: 113–117, 2011.

[66] Alan D. Martin. Kaon - Nucleon Parameters. *Nucl. Phys.*, B179:33, 1981.

[67] M. Iwasaki, R.S. Hayano, T.M. Ito, S.N. Nakamura, T.P. Terada, et al. Observation of the kaonic hydrogen K(alpha) x-ray. *Phys.Rev.Lett.*, 78:3067–3069, 1997.

[68] T.M. Ito, R.S. Hayano, S.N. Nakamura, T.P. Terada, M. Iwasaki, et al. Observation of kaonic hydrogen atom x rays. *Phys.Rev.*, C58:2366–2382, 1998.

[69] J.R. Taylor. *Scattering Theory: The Quantum Theory of Nonrelativistic Collisions.* American Institute of Physics, 1973.

[70] R.J. Eden and J.R. Taylor. Poles and Shadow Poles in the Many-Channel S Matrix. *Phys.Rev.*, 133:B1575–B1580, 1964.

[71] B.C. Pearce and B.F. Gibson. Observable Effects of Poles and Shadow Poles in Coupled Channel Systems. *Phys.Rev.*, C40:902–911, 1989.

[72] Yoichi Ikeda, Hiroyuki Kamano, and Toru Sato. Energy dependence of barkn interactions and resonance pole of strange dibaryons. *Prog. Theor. Phys.*, 124:533–539, 2010.

Appendix A

The transformation relation from 10 channel base to isoscalar base:

$$C_{1,1}^{\text{iskal}} = \frac{1}{3}(C_{2,2} + 2 \cdot C_{2,3} + 2 \cdot C_{2,4} + C_{3,3} + 2 \cdot C_{3,4} + C_{4,4})$$

$$C_{1,2}^{\text{iskal}} = -\frac{1}{\sqrt{6}}(C_{2,5} + C_{3,5} + C_{4,5} + C_{2,6} + C_{3,6} + C_{4,6})$$

$$C_{1,3}^{\text{iskal}} = -\frac{1}{\sqrt{3}}(C_{2,7} + C_{3,7} + C_{4,7})$$

$$C_{1,4}^{\text{iskal}} = \frac{1}{\sqrt{6}}(C_{2,9} + C_{3,9} + C_{4,9} + C_{2,10} + C_{3,10} + C_{4,10})$$

$$C_{2,2}^{\text{iskal}} = \frac{1}{2}(C_{5,5} + 2 \cdot C_{5,6} + C_{6,6})$$

$$C_{2,3}^{\text{iskal}} = \frac{1}{\sqrt{2}}(C_{5,7} + C_{6,7})$$

$$C_{2,4}^{\text{iskal}} = -\frac{1}{2}(C_{5,9} + C_{5,10} + C_{6,9} + C_{6,10})$$

$$C_{3,3}^{\text{iskal}} = C_{7,7}$$

$$C_{3,4}^{\text{iskal}} = -\frac{1}{\sqrt{2}}(C_{7,9} + C_{7,10})$$

$$C_{4,4}^{\text{iskal}} = \frac{1}{2}(C_{9,9} + 2 \cdot C_{9,10} + C_{10,10}).$$

The transformation relation from 10 channel base to isovector base:

$$C_{1,1}^{\text{ivec}} = C_{1,1}$$

$$C_{1,2}^{\text{ivec}} = \frac{1}{\sqrt{2}}(C_{1,3} - C_{1,2})$$

$$C_{1,3}^{\text{ivec}} = -C_{1,4}$$

$$C_{1,4}^{\text{ivec}} = C_{1,5}$$

$$C_{1,5}^{\text{ivec}} = -C_{1,6}$$

$$C_{2,2}^{\text{ivec}} = \frac{1}{2}(C_{2,2} + C_{3,3} - 2 \cdot C_{2,3})$$

$$C_{2,3}^{\text{ivec}} = \frac{1}{\sqrt{2}}(C_{2,4} - C_{3,4})$$

$$C_{2,4}^{\text{ivec}} = -\frac{1}{\sqrt{2}}(C_{3,5} - C_{2,5})$$

$$C_{2,5}^{\text{ivec}} = \frac{1}{\sqrt{2}}(C_{2,6} - C_{3,6})$$

$$C_{3,3}^{\text{ivec}} = C_{4,4}$$

$$C_{3,4}^{\text{ivec}} = -C_{4,5}$$

$$C_{3,5}^{\text{ivec}} = -C_{4,6}$$

$$C_{4,4}^{\text{ivec}} = C_{5,5}$$

$$C_{4,5}^{\text{ivec}} = -C_{5,6}$$

$$C_{5,5}^{\text{ivec}} = C_{6,6}$$

Since the coupling coefficients are symmetric $C_{ij} = C_{ji}$, we show only above diagonal terms.

Appendix B
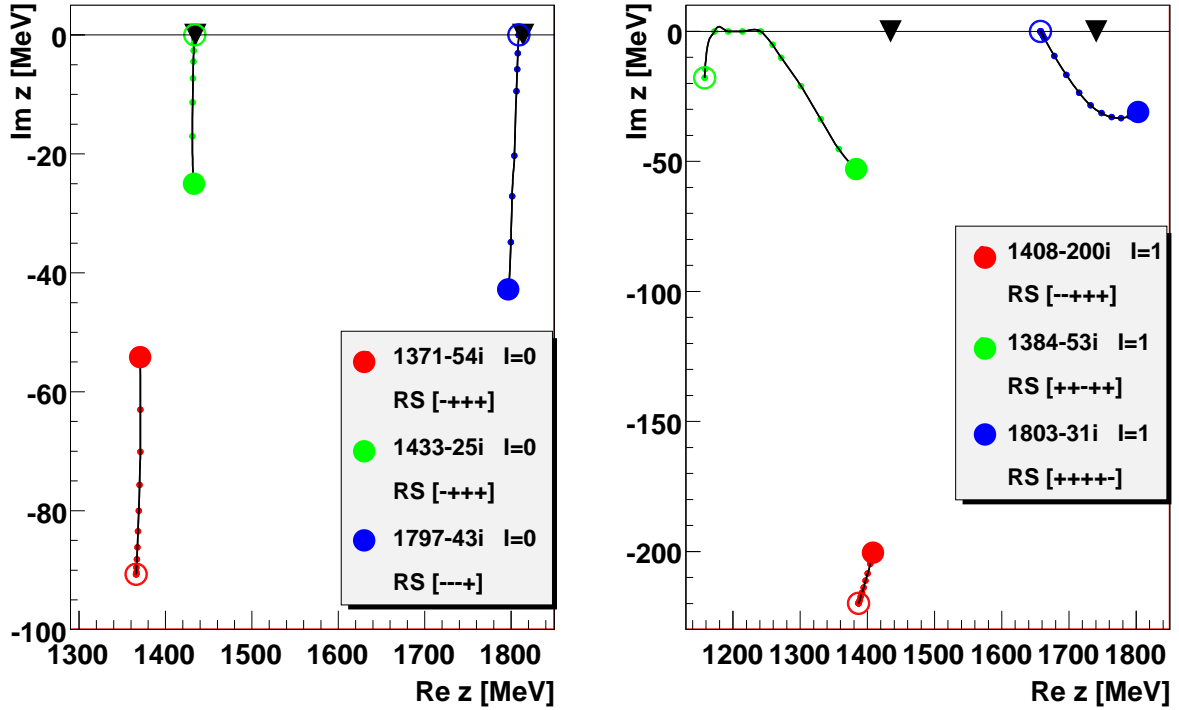
Figure 1: Pole movements upon scaling the nondiagonal interchannel couplings in the TW1 model. Left panel: isoscalar states ($I = 0$), right panel: isovector states ($I = 1$). The large solid and empty circles show the pole positions in the physical and zero coupling limits, respectively. The black triangles mark the $\bar{K}N$ and $K\Xi$ thresholds in the isoscalar case and the $\bar{K}N$ and $\eta\Sigma$ thresholds in the isovector case. Energies of the thresholds are $E_{\bar{K}N} = 1434.6$ MeV, $E_{\eta\Sigma} = 1740.6$ MeV and $E_{K\Xi} = 1814.0$ MeV. The Riemann sheets the poles move on are specified in the legend.
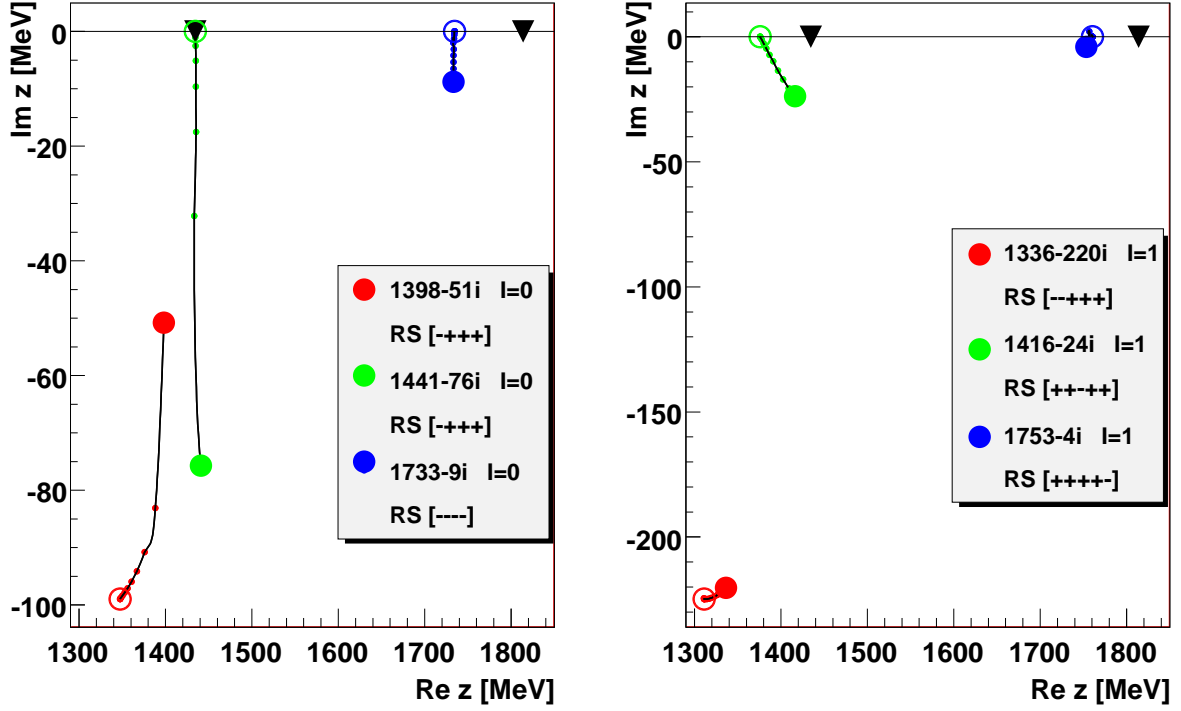
Figure 2: Pole movements upon scaling the nondiagonal interchannel couplings in the CS30 model. Left panel: isoscalar states ($I = 0$), right panel: isovector states ($I = 1$). The large solid and empty circles show the pole positions in the physical and zero coupling limits, respectively. The black triangles mark the $\bar{K}N$ and $K\Xi$ thresholds. Energies of the thresholds are $E_{\bar{K}N} = 1434.6$ MeV, $E_{\eta\Sigma} = 1740.6$ MeV and $E_{K\Xi} = 1814.0$ MeV. The Riemann sheets the poles move on are specified in the legend.